

STAR FORMATION IN THE FIELD AND CLUSTERS OF NGC 5253 <sup>1</sup>CHRISTY A. TREMONTI <sup>2,3</sup>  
cat@pha.jhu.eduDANIELA CALZETTI<sup>3</sup>  
calzetti@stsci.eduCLAUS LEITHERER<sup>3</sup>  
leitherer@stsci.edu

AND

TIMOTHY M. HECKMAN<sup>2,3</sup>  
heckman@pha.jhu.edu  
*accepted for publication in ApJ*

## ABSTRACT

We investigate the star formation history of both the bright star clusters and the diffuse ‘field star’ population in the dwarf starburst galaxy NGC 5253 using longslit ultraviolet spectroscopy obtained with the Space Telescope Imaging Spectrograph (STIS). The slit covers a physical area of  $370 \times 1.6$  pc and includes 8 apparent clusters and several inter-cluster regions of diffuse light which we take to be the field. The diffuse light spectrum lacks the strong O-star wind features which are clearly visible in spectra of the brightest clusters. This discrepancy provides compelling evidence that the diffuse light is not reflected light from nearby clusters, but originates in a UV-bright field star population, and it raises the issue of whether the star formation process may be operating differently in the field than in clusters. We compare our spectra to STARBURST99 evolutionary synthesis models which incorporate a new low metallicity ( $\sim 1/4 Z_{\odot}$ ) atlas of O-star spectra. The clusters are well fit by instantaneous burst models with a Salpeter initial mass function (IMF) extending up to  $100 M_{\odot}$ , and we derive ages for them ranging from 1 to 8 Myrs. Reasonable fits to the field spectrum are obtained by continuous star formation models with either an upper mass cut-off of  $\sim 30 M_{\odot}$  or an IMF slope steeper than Salpeter ( $\alpha \sim 3.5$ ). We favor a scenario which accounts for the paucity of O-stars in the field without requiring the field to have a different IMF than the clusters: stellar clusters form continuously and then dissolve on  $\sim 10$  Myr timescales and disperse their remaining stars into the field. We consider the probable contribution of an O-star deficient field population to the spatially unresolved spectra of high redshift galaxies.

*Subject headings:* galaxies: starburst—galaxies: individual (NGC 5253)—galaxies: galaxies: star clusters—galaxies: stellar content

## 1. INTRODUCTION:

The energy produced in the star formation process is distributed over some 10 decades of frequency, from the X-ray to the radio; however, the bulk of our knowledge about high redshift ( $z \gtrsim 2.5$ ) star forming galaxies comes from a rather limited observational window: the rest-frame ultraviolet. This is a consequence of the simple fact that high redshift galaxies are faint (at  $z \sim 3$   $L^*$  corresponds to  $R \simeq 24.5$ , (Steidel et al. 1999)) and thus accessible only in spectral regimes where the sensitivity is optimum. At present most observations of high- $z$  galaxies are made by large ground-based telescopes working in the visible, which corresponds to the rest-frame ultraviolet for galaxies at redshifts larger than  $\sim 2.5$ .

Fortuitously, the ultraviolet (UV) is an excellent regime in which to study star forming galaxies: it contains the direct spectroscopic signatures of the hot young massive stars which dominate the bolometric light, as well as an abundance of interstellar features that provide valuable probes of the gas. In fact, almost all of the relevant stellar

and interstellar absorption lines have wavelengths below 3000 Å. The full diagnostic power of this rich spectral region is still being realized: a number of programs are underway to correlate UV spectral morphology with global galaxy parameters such as mass, metallicity, extinction, stellar content, and bolometric luminosity (e.g. Heckman et al. 1998; Meurer, Heckman & Calzetti 1999; Adelberger & Steidel 2000). These studies concentrate on local starburst galaxies whose global properties are well known from observations in a number of wavebands.

Nearby starburst galaxies are the most obvious local counterparts of the high redshift galaxies currently being found in large numbers through color selection based on the Lyman break technique (e.g. Steidel et al. 1996, 1999). While the extinction corrections to the rest-frame ultraviolet of high- $z$  galaxies are still a matter of some debate, it is clear that the stellar surface mass densities and star formation rates per unit area of these galaxies are several orders of magnitude higher than ordinary late type galaxies, and are comparable to those of local starbursts (Meurer

<sup>1</sup> Based on observations with the NASA/ESA Hubble Space Telescope, obtained at the Space Telescope Science Institute, which is operated by the Association of Universities for Research in Astronomy, Inc. under NASA contract No. NAS5-26555.

<sup>2</sup> Department of Physics & Astronomy, The Johns Hopkins University, 3400 N. Charles Street, Baltimore, MD 21218

<sup>3</sup> Space Telescope Science Institute, 3700 San Martin Drive, Baltimore, MD 21218

et al. 1997; Kennicutt et al. 1998). Local starbursts and Lyman-dropout galaxies share similar distributions of observed UV colors (Meurer et al. 1997; Meurer, Heckman & Calzetti 1999; Adelberger & Steidel 2000) and have spectral morphologies which are characterized by blue continua with strong interstellar absorption, the broad P-Cygni signatures of stellar winds, and weak Ly- $\alpha$  emission (Steidel et al. 1996; Lowenthal et al. 1997; Pettini et al. 2000).

High-resolution UV spectra of local starburst galaxies provide invaluable templates for comparison with spectra of high- $z$  galaxies. However, *such comparisons must be viewed with a note of caution because of differences in spatial resolution.* High redshift galaxies have small angular sizes and spectra which are spatially integrated, whereas local starbursts have such large angular scales that only select pieces of the burst can be sampled without using apertures so large as to substantially degrade the spectral resolution. Differences in the spatial resolution of high and low- $z$  observations are particularly significant because bursts of star formation are known to be highly inhomogeneous. Space-based UV imaging has shown nearby star forming regions to be composed of compact, young, UV-bright stellar clusters embedded in a diffuse, irregular, UV background (Meurer et al. 1995).

Historically, high-resolution UV spectroscopy of local starburst galaxies has focused on individual stellar clusters because of their high surface brightness. However, *the UV-bright clusters are not the dominant contributors to the UV luminosity of a starburst galaxy:* the diffuse UV light typically accounts for  $\sim 50\%$  to  $80\%$  of the total (Buat et al. 1994; Meurer et al. 1995; Maoz et al. 1996). The nature of the diffuse UV component is hinted at by UV images of the nearest starbursts where individual high mass stars are resolved (Meurer et al. 1995). These stars appear to trace the diffuse light isophotes, suggesting that the diffuse light is not simply reflected light from the bright clusters, but originates in a UV-bright field star population. This raises the issue of whether or not there are two distinct ‘modes’ of star formation operating in a starburst: one which produces compact clusters and one which produces more diffuse star formation. What is clear is that a starburst is not the same thing as a star cluster; nor is it the sum of its clusters. The diffuse light represents a large, if not dominant, part of the integrated light of a starburst, and may represent an important and distinct mode of star formation.

Understanding the nature of the diffuse UV component is one of the principal aims of our present investigation which utilizes STIS longslit ultraviolet spectroscopy of the central starburst in the nearby galaxy NGC 5253. By addressing the contribution that both the clusters and the diffuse light make to the integrated spectrum of a local galaxy, we hope to be able to more accurately interpret the spatially unresolved spectra of high- $z$  star forming galaxies.

## 2. BACKGROUND

NGC 5253 is a metal-poor dwarf galaxy in the Centaurus Group which contains an extremely young starburst. A re-calibration of existing Cepheid data by the *HST* Key Project on the Extragalactic Distance Scale team has produced an improved distance estimate to the

galaxy of  $3.33 \pm 0.29$  Mpc (Gibson et al. 2000;  $1'' \approx 16$  pc). NGC 5253 has been the target of a number of observational programs at wavelengths ranging from the X-ray to the radio, the results of which are summarized by Caldwell & Phillips (1989), Martin & Kennicutt (1995), and Calzetti et al. (1997, 1999). The metallicity of NGC 5253 is  $\sim \frac{1}{5} Z_{\odot}$  (Kobulnicky, Kennicutt, & Pizagno 1999) and is relatively constant across the galaxy, with the exception of a few areas of enhanced nitrogen abundances (Walsh & Roy 1989; Kobulnicky et al. 1997). NGC 5253’s small size and modest metallicity make it an excellent analogue to galaxies in their early phases of formation, while its proximity makes it ideal for disentangling the diffuse UV light from that of the bright stellar clusters.

Our long slit traverses a relatively large portion of NGC 5253, as can be seen in Figure 1. Morphologically the galaxy is somewhat unusual (termed ‘amorphous’ by Sandage & Brucato (1979)). Various authors have suggested that NGC 5253 may have resembled a dwarf elliptical until an encounter with NGC 5236 (M83) one to two Gyrs ago triggered the formation of a new stellar population (Rogstad, Lockart, & Wright 1974; Caldwell & Phillips 1989). Star formation is ongoing in the central  $20''$  ( $\sim 325$  pc) of the galaxy which contains a dozen UV-bright stellar clusters (Meurer et al. 1995) and is very blue except where dust produces patchy, heavy obscuration (Calzetti et al. 1997). A prominent dust lane with  $A_V \gtrsim 2.2$  mags girds the galaxy nearly perpendicular to its major axis (Calzetti et al. 1997). Radio observations suggest that a large fraction of the most recent star formation is hidden by dust (Turner, Ho, & Beck 1998). The ionized gas in NGC 5253 is more extended by a factor of  $\sim 2$  than the continuum emission, and it is circularly symmetric about a stellar cluster (NGC5253-5 of Calzetti et al. 1997) which is located near the geometric center of the galaxy.

The most active region of star formation is the starburst nucleus, which is 40 – 50 pc in size and centered at the position of the H $\alpha$  peak. An age as young as 5 Myr is suggested by the large H $\alpha$  equivalent width (Calzetti et al. 1999), the presence of Wolf-Rayet stars (Campbell, Terlevich & Melnick 1986; Walsh & Roy 1987, 1989; Schaerer et al. 1997), the small number of red supergiants (Campbell & Terlevich 1984), and the purely thermal component of the radio emission (Beck et al. 1996). Stars in this nuclear region are still embedded in the parental cloud with  $A_V \sim 9 - 35$  mag (Calzetti et al. 1997). Recent observations at 1.3 and 2 cm have revealed the presence of a  $\sim 1-2$  pc ‘supernebula’ — a very young and gas-rich counterpart of a super-star cluster — which may be the youngest globular cluster known (Turner, Beck, & Ho 2000). The star formation rate density in the nuclear region is between  $10^{-5}$  and  $10^{-4} M_{\odot} \text{ yr}^{-1} \text{ pc}^{-2}$  (Calzetti et al. 1999), which corresponds to the maximum levels observed in starburst galaxies (Meurer et al. 1997). However, the bulk of the observed UV light is not produced by the starburst nucleus, but by the surrounding regions (extending out to 250 pc), which are older, relatively unextincted, and producing stars at a rate 10 times lower than that of the nuclear starburst (Calzetti et al. 1997).

## 3. OBSERVATIONS AND DATA REDUCTION

We obtained longslit ultraviolet spectra of the central region of NGC 5253 with the Space Telescope Imaging Spectrograph (STIS) aboard the *Hubble Space Telescope* on 1999 July 27. We utilized the  $52'' \times 0.1''$  slit and the G140L grating to obtain the best compromise between throughput and spectral resolution. The spectra span a wavelength range of 1150 – 1700 Å with a resolution of  $\sim 2$  Å, which provides a good match to our stellar evolutionary synthesis models (1200 – 1600 Å;  $\delta\lambda \sim 1.5$  Å).

The position of the slit was chosen so as to intersect Clusters 2, 3, and 5 of Calzetti et al. 1997 (see Figure 1). Target acquisition was accomplished in a two phase process utilizing the STIS CCD at visible wavelengths. First, a bright foreground star 1.4 from Cluster 5 was acquired in a  $5''$  field of view and centered on the CCD to an accuracy of  $\pm 0''.01$ . An offset was then performed to Cluster 5 (RA =  $13^{\text{h}}39^{\text{m}}56^{\text{s}}.02$ , Dec =  $-31^{\circ}38'25''.0$ , J2000) and a peakup was done to refine the centering. The spacecraft moved the slit across the target parallel to the dispersion direction in five  $0''.075$  steps. The optimal spacecraft location (accurate to 5% of the slit,  $\sim 0''.005$ ) was determined from a flux weighted centroid algorithm. The slit orientation (PA =  $56^{\circ}246$ ) was dictated by Clusters 2 and 3, which are separated by  $< 1''$  and are  $\sim 8''$  distant from Cluster 5.

Following the successful target acquisition, the G140L grating was moved into the beam and four frames of duration 1410, 2945, 2945, and 2945 seconds were obtained with the STIS FUV-MAMA detector. The data were processed with the Space Telescope Science Institute’s *CALSTIS* pipeline, which provides automated rebinning, global detector linearity correction, dark subtraction, flat fielding, wavelength calibration, and conversion to absolute flux units. For our subsequent analysis we utilized the fully calibrated two-dimensional images produced by the pipeline, which are rectified to be linear in both the wavelength and spatial dimension. After examining the four calibrated frames for spatial shifts, we combined them into a single two-dimensional image using the IRAF task *mscombine*.

The slit traverses roughly 370 pc of NGC 5253, including both the intense regions of star formation near the nucleus and the more quiescent outer regions (see Figure 1). The spatial dimension of the data extends  $23''$  with an image scale of  $0''.0244 \text{ pixel}^{-1}$  ( $\sim 0.4 \text{ pc pixel}^{-1}$ ), which is sufficient to resolve stellar clusters. Figure 2 shows the integrated 1150 – 1710 Å flux as a function of slit position. A number of bright point-like sources are visible, embedded within a  $\sim 300$  pc plateau of diffuse light. For our subsequent analysis, we define the 8 brightest peaks along the spatial axis to be clusters, and take regions between those peaks to be the field or diffuse component. (We use the terms ‘cluster’ and ‘field’ quite liberally here.) Data within these subregions were binned into one-dimensional spectra.

The spatial pixels binned up to form a given cluster’s spectrum were chosen by eye from an examination of the spectrally integrated data shown in Figure 2. The spectral properties of the fainter clusters were fairly sensitive to the boundaries chosen. We made a concerted effort to balance the competing demands of signal-to-noise (S/N) and spectral purity by examining the effects that broadening the

extraction had on the resultant spectrum. Some of our so-called clusters may nevertheless include more than one coeval population (note the two component blended profile of Cluster 5 in Figure 2). The extracted spectra of the four brightest clusters are shown in Figure 3.

Because of their greater extent, the field regions were not nearly as sensitive to their spatial boundaries. However, subtle differences were apparent when large areas were considered. We therefore defined three distinct field regions (shown in Figure 2), each with a S/N comparable to that of the brightest clusters. The extracted field spectra are shown in Figure 4.

The low redshift of NGC 5253 ( $v = 404 \text{ km s}^{-1}$ ) precluded direct measurement of our spectral resolution because the strong interstellar features of the starburst are blended with intervening Milky Way absorption lines. We therefore estimate our resolution based on the known properties of STIS. At the distance of NGC 5253, a typical cluster is neither a point source nor a fully extended source, so we expect our spectral resolution to be intermediate between point and extended source values (0.9 Å and 2.4 Å respectively). We estimate a value of  $\sim 1.8$  Å as an appropriate resolution for our cluster spectra. Our field spectra should have the resolution of a fully extended source. We measure a 2.2 Å FWHM for the Lyman- $\alpha$  airglow line.

Because the clusters are embedded in a diffuse background and are resolved, we treated all of our spectra as extended continuum sources when converting from units of surface brightness in the two-dimensional image to units of flux ( $\text{ergs s}^{-1} \text{ cm}^{-2} \text{ \AA}^{-1}$ ) in the one-dimensional extracted spectra. Treating the clusters as point sources would increase their measured fluxes by approximately a factor of two due to corrections for the extended wings of the PSF.

The extracted spectra were corrected for slight relative wavelength shifts (0.02 – 0.2 Å) based on the peak geocoronal Ly- $\alpha$  emission, de-redshifted, and then rebinned to the model resolution of 0.75 Å per pixel. We then corrected the spectra for the strong geocoronal emission at Ly- $\alpha$  and O I  $\lambda 1302$ . Data in a region at the edge of the diffuse light plateau (the region labeled “sky” in Figure 2) were extracted to produce a one-dimensional spectrum. While this spectrum included substantially more pixels than any of the field regions, the stellar features were extremely faint, making it a suitable “sky” spectrum. We subtracted a weak continuum from the sky spectrum and set all the pixels to zero except for a 40 Å window around Ly- $\alpha$  and a 20 Å window around O I. Taking this to be a purely geocoronal spectrum, we then subtracted it from the 1-dimensional spectra of the cluster and field regions in proportion to the number of pixels covered by each. The intrinsic interstellar absorption lines of O I and Si II near  $\lambda 1302$  Å appear to be fairly well recovered.

Extinction corrections were applied individually to each of the unrectified spectra. We removed the foreground Galactic extinction with the standard Milky Way extinction law of Cardelli, Clayton, & Mathis (1989), using a reddening of  $E(B-V) = 0.05$  (Burstein & Heiles 1982) for all of the spectra. The extinction intrinsic to the starburst was removed using the starburst obscuration curve (Calzetti et al. 2000, and references therein). Assuming a foreground dust geometry with a standard extinction curve (e.g. the Milky Way or LMC curve) would generally

give a similar or lower color excess than the values derived with the starburst obscuration curve. However, the differences would be small in the present case, owing to the modest reddening affecting the stellar clusters (with the exception of Cluster 5 which is discussed further in §5.1, and possibly Cluster 8.)

We used  $\beta$ , the power law slope of the UV continuum ( $F \propto \lambda^\beta$ ), as a diagnostic of the reddening internal to the starburst. Because of the plethora of weak lines in the spectra, the value of  $\beta$  measured was fairly sensitive to the method of continuum fitting. We used 10 iterations of a sigma rejection routine with a  $2.0\sigma$  lower bound and a  $3.5\sigma$  upper bound to perform a power law fit over the wavelength range 1240 – 1600 Å. This method produces systematically shallower slopes than the method of Calzetti, Kinney & Storchi-Bergmann (1994) in which a fit is performed over 10 line-free windows (only 5 of which are in our wavelength range.) However, in this instance we are not concerned with the absolute value of  $\beta$ , merely the difference in  $\beta$  between the data and the models, which are free of reddening. For a wide range of model parameters (detailed in §4), we measure  $\beta$  values of -2.50 to -2.75. Since our measurements are probably not accurate to more than  $\pm 0.1$ , we take -2.6 to be the intrinsic slope of the UV continuum for all of our spectra. We derive  $E(B-V)$  values for each of the cluster and field regions by de-reddening the observed spectrum using the starburst obscuration law until the measured value of  $\beta$  is -2.6. The observed  $\beta$  values for each of the cluster and field regions are listed in Tables 1 and 3. Table 2 contains the  $\beta$  values of the clusters corrected for galactic foreground reddening and the derived color excess.

#### 4. MODELING

We compare the spectra of the clusters and the field to the *STARBURST99* stellar evolutionary synthesis models (Leitherer et al. 1999). The *STARBURST99* models (hereafter SB99) have been optimized to reproduce many spectrophotometric properties of galaxies with active star formation. We briefly describe those aspects of the models which we utilize in §4.1; in §4.2 we describe our input model parameters; and in §4.3 we describe our fitting routine.

##### 4.1. *STARBURST99*

The SB99 models use two limiting cases of the star-formation law: an instantaneous burst with no subsequent star formation and star formation proceeding continuously at a constant rate. Stellar populations are parameterized by their stellar initial mass function (IMF), which is assumed to be a power law ( $\Phi \propto \int_{M_{low}}^{M_{up}} m^{-\alpha} dm$ ) between a lower mass cut-off ( $M_{low}$ ) and an upper mass cut-off ( $M_{up}$ ). The stellar population is evolved from the ZAMS using the evolutionary models of the Geneva group. Luminosity, effective temperature, and radius are calculated for each star during each evolutionary time step ( $10^4$  years). Spectral types are determined, and an appropriate ultraviolet spectrum (1200 – 1600 Å) is assigned to each star from a stellar library. The resultant model spectra are simply a combination of the constituent stellar spectra at each time step.

The library spectra utilized by SB99 are composite stellar spectra with signal-to-noise ratios of  $\sim 20$ . The original library consisted of spectra created from high dispersion (0.75 Å) IUE observations of solar or slightly sub-solar metallicity Milky Way stars, with O and Wolf-Rayet star spectra drawn from the atlas of Robert, Leitherer, & Heckman (1993) and B-star spectra from de Mello, Leitherer, & Heckman (2000). In this study we take advantage of an important and very recent addition to the SB99 library: an atlas of metal poor ( $\sim 1/4 Z_\odot$ ) O-star spectra created from HST observations of stars in the Large (LMC) and Small (SMC) Magellanic Clouds (Leitherer et al. 2001).

##### 4.2. Model Parameters

We compare our data to SB99 models with a variety of star formation scenarios. The high mass stellar content of a starburst depends upon both the slope of the initial mass function,  $\alpha$ , and the upper mass cut-off of the IMF,  $M_{up}$ . Populations which form in an instantaneous burst will also have a dependence on age, since the most massive stars are the shortest lived. We construct three grids of models where two of these three parameters ( $\alpha$ ,  $M_{up}$ , and age) are held fixed and the third is allowed to vary.

Our benchmark model is an instantaneous burst with a Salpeter IMF slope  $\alpha = 2.35$ , a lower mass cut-off of  $M_{low} = 1 M_\odot$ , and an upper mass cut-off of  $M_{up} = 100 M_\odot$ . We allow this model to evolve from 0 – 50 Myrs and create a grid of spectra with ages in 1 Myr increments. The parameters of our instantaneous burst model are in line with results from recent studies that have shown the high-mass end ( $M \geq 5 M_\odot$ ) of the IMF to be remarkably uniform in both resolved regions of active star formation (Massey 1998; Massey, Johnson, & Degioia-Eastwood 1995; Hunter et al. 1996) and in starbursts (Garcia-Vargas, Bressan, & Diaz 1995; Stasinska & Leitherer 1996). The high-mass end slope in stellar clusters is measured to be  $\alpha \approx 2.3-2.5$  (e.g., Scalo 1998), which is, for all practical purposes, a ‘Salpeter slope’, and the upper mass cut-off is  $>70-100 M_\odot$  (Massey 1998). No systematic variations in the IMF slope are observed over about a factor 10 in metallicity and a factor  $\sim 1000$  in stellar density (Massey et al. 1995; Massey, Johnson, & Degioia-Eastwood 1995). In this study we are not particularly concerned with the low end of the IMF, except for cluster mass determinations (see § 5.1), as our UV spectroscopy is insensitive to the low-mass cut-off. We have tested that low-end-truncated IMFs up to  $10 M_\odot$  do not induce a significant variation in the UV spectral features of our models, and, thus, in the cluster age determinations.

We also consider continuous star formation models. Continuous models take approximately 10 Myr to equilibrate, after which the UV spectrum changes very little as a function of age. We therefore fix the age at 50 Myr and let the free parameters be the IMF slope and the upper mass cut-off. We create 2 grids of continuous models: one with  $\alpha = 2.35$ ,  $M_{low} = 1$ , and  $M_{up} = 10, 20, 30, 40, 50, 100 M_\odot$  and the other with  $M_{low} = 1 M_\odot$ ,  $M_{up} = 100 M_\odot$ , and  $\alpha = 2.35, 3, 3.5, 4, 5$ . Continuous star formation models should be more appropriate to star formation occurring in spatially extended regions such as the stellar field, where the crossing times are long, typically of order 10 Myr.

For all of our SB99 models, we used an evolutionary

track metallicity of  $0.2 Z_{\odot}$  ( $Z_{\odot} = 0.02$ , by mass) and the new LMC/SMC stellar libraries. This provides a good match to the metallicity of NGC 5253's gas which is known to be  $\sim \frac{1}{5} Z_{\odot}$ . The good agreement between the metallicity of our data and that of the stellar libraries is particularly important because the age and IMF sensitive features also have a Z-dependence, with the general trend being towards weaker lines at lower metallicity (Leitherer et al. 2001). In particular, the strength of the P-Cygni features depends upon the mass loss rate which is a function of metallicity (e.g. Puls et al. 1996). This dependence is evident in comparisons of stars of the same spectral type and luminosity class in the Milky Way, LMC, and SMC (e.g. Garmany & Conti 1985; Walborn et al. 1995, 2000).

One important caveat is that the low metallicity library employed by SB99 extends only from O3 through B0, with all other spectral groups being drawn from the original solar metallicity library. This metallicity mismatch between the high mass stars and intermediate and low mass stars can affect the computed synthetic spectrum of a composite population depending on its age or IMF. The line profiles of the stellar wind lines, which are produced primarily in very massive stars ( $> 40 M_{\odot}$ ), are not much affected, while the continuum and many photospheric lines are more sensitive to contributions from B stars. Leitherer et al. (2001) conclude that for populations with a standard Salpeter IMF up to  $100 M_{\odot}$  the effect of the solar metallicity B-stars is relatively minor for continuous star formation models or instantaneous bursts with ages less than  $\sim 10$  Myr. This is discussed further in §5.2.

#### 4.3. Model Fitting

The ultraviolet spectrum of a star forming region provides a sensitive measure of its high-mass star content because the most massive stars are also the most luminous, and they dominate the integrated light. Figure 5 contrasts the O-star dominated composite cluster spectrum with the B-star dominated spectrum of the field. An O-star dominated spectrum is characterized by the broad ( $\sim 2000 \text{ km s}^{-1}$ ) stellar wind P-Cygni profiles of N V  $\lambda 1240$ , Si IV  $\lambda 1400$ , and C IV  $\lambda 1550$ . These features are notably absent in B-star dominated spectra, which exhibit increasingly strong narrow ( $\sim 350 \text{ km s}^{-1}$ ) photospheric features, such as Si II  $\lambda 1265$  and Si II  $\lambda 1309$ . Our data have sufficient S/N ( $\sim 10$ ) and spectral resolution ( $\sim 2 \text{ \AA}$ ) to allow us to utilize these stellar features as probes of the massive star content in various regions of NGC 5253.

We determined which models provided the best fit to our cluster and field spectra in the  $1200 - 1600 \text{ \AA}$  regime using an automated routine that takes as input the extinction corrected spectrum of a cluster or field region, a grid of SB99 model spectra, and an array of values corresponding to the free variable in the grid of models (i.e. the age, IMF slope, or  $M_{up}$ .) For each of the model spectra in the grid the goodness of the fit is characterized by a  $\chi^2$  value computed in the following manner:  $\chi^2 = (o_i - m_i)^2 w_i / \sigma_i^2$ , where  $o_i$  represents the observed data for the  $i$ th pixel,  $m_i$  the model data,  $\sigma_i$  the error in the observed spectrum, and  $w_i$  the assigned weight.

Weights were applied in order to maximize the sensitivity of the  $\chi^2$  to regions of the spectrum which are most

influenced by the age/stellar content of the burst, namely the stellar wind lines. On the basis of the detailed line analysis of de Mello et al. (2000), we classified each pixel in our spectra as belonging to either the continuum, an interstellar line, or a stellar wind line, and assigned weights accordingly. The interstellar lines were given a weight of zero; the 470 pixels of continuum a weight of 1; and the 69 pixels corresponding to stellar wind lines a weight of 10. The result of this weighting scheme was to eliminate the interstellar lines from consideration, and to give the wind lines a weight  $\sim 1.5$  times greater than that of the continuum.

It was necessary to eliminate the interstellar absorption lines from our  $\chi^2$  because SB99 is designed to model the integrated UV light of a purely *stellar* population; no consideration is given to the gaseous environment of the star-forming region. Interstellar absorption lines are present in the models only in so much as they are present in the library of stellar spectra. Unfortunately, nearly all of the features which are sensitive diagnostics of the stellar population have some interstellar contamination. In the case of the broad stellar wind features, we attempt to mask out the narrow interstellar core (see Figure 5). However, the separation of stellar and interstellar features remains a source of uncertainty.

Our routine returns the best fit model (minimum  $\chi^2$ ) and plots the evolution of the  $\chi^2$  with the free parameter, as shown in Figure 6. The best fits proved to be relatively robust to the method of  $\chi^2$  evaluation: small changes in the weighting scheme employed had virtually no effect, especially in cases where the S/N was good or O-star wind lines were still present. In order to quantify the error associated with our best fit models, we utilized the bootstrap method. This entailed randomly resampling the residuals of the best fit, adding these to the model spectrum, and running the resultant spectrum through our automated fitting routine. This procedure was repeated 1000 times for each spectrum. The error bars associated with the 90% confidence interval were derived from a histogram of the results.

## 5. ANALYSIS

### 5.1. Clusters

The regions of the spectrum that we define as clusters are shown in Figure 2. Our definition of what constitutes a 'cluster' is clearly somewhat arbitrary: we have taken the eight brightest peaks in the spectrum. Our clusters are not necessarily bound entities, but we retain this labeling for simplicity. For consistency we use the cluster naming convention of Calzetti et al. 1997 for Clusters 2, 3, and 5, and number the remaining clusters (starting with 7) in order of decreasing observed flux. The extracted spectra of the four brightest clusters are shown in Figure 3. The measured properties of the clusters are reported in Table 1.

All of our clusters, except for Cluster 8, have spatial profiles that are clearly resolved (their gaussian FWHM values are well in excess of the 1.6 pixels expected for a point source at  $1400 \text{ \AA}$ ) and relatively symmetric. Cluster 8 is actually a collection of a few peaks of UV emission covering 13 pixels (5.2 pc). The most prominent of these peaks extends no more than four pixels and is compatible with a point source. Its UV luminosity,  $L_{1500} \simeq 5 \times 10^{35} \text{ ergs s}^{-1}$ ,

could be produced by a single O-supergiant, but the observed spectral features are more consistent with those of a B-star. We calculate that 3–4 B supergiants could produce the observed UV luminosity, implying that Cluster 8 is actually an association with a modest number of stars.

We compared our dereddened cluster spectra to a grid of instantaneous burst models with a Salpeter IMF slope ( $\alpha = 2.35$ ), an upper mass cut-off of  $100 M_{\odot}$ , and ages ranging from 0 to 50 Myr in 1 Myr increments. An instantaneous burst model is appropriate for the clusters since they have typical half light radii of 0.6 parsecs, and thus have negligibly short crossing times, of order 0.1 Myr. All eight cluster spectra were remarkably well fit by the models. The four brightest clusters are shown with their best fitting models in Figure 7. We assign ages to the clusters on the basis of their best fits and error bars on these ages which represent the 90% confidence interval (see §4.3 for details). The robustness of our age determination can also be assessed by examining the shape of the  $\chi^2$  evolution, shown in Figure 6 for Clusters 2, 3, 5, and 7. The ages of the other clusters are expected to be more uncertain than the formal error bars reflect since they are less luminous and potentially subject to strong stochastic effects if only a handful of O-stars are present. The ages and other model dependent properties of the clusters are summarized in Table 2.

We derive cluster masses from the dereddened luminosity of the clusters. For the 4 brightest clusters (2, 3, 5, 7) we derive fluxes from photometry of an archival WFPC2 image in the F170W filter. The signal-to-noise of the image (a combination of two 400 second images) is too low for the remaining clusters to be clearly detected. We have corrected our F170W image for warm pixels, decontamination events, geometric distortion, and charge transfer efficiency. The photometry we obtain provides a more accurate estimate of the total luminosity of the clusters since they are extended objects and their exact position relative to the slit is unknown. In the most extreme case, Cluster 3, the luminosity derived from the photometry is a factor of  $\sim 30$  greater than that obtained from our STIS spectrum. The masses of the four clusters too faint to be detected in the F170W image (8, 9, 10, 11) are therefore lower limits.

All of the clusters have been de-reddened as described in §3 using the starburst obscuration curve (Calzetti et al. 2000). This assumption provides a lower limit to the actual dust obscuration (and hence a lower limit to the dereddened UV luminosity and mass) if more complex geometries, such as dust mixed with stars, are present. To clarify the magnitude of the effect we use as an example the most reddened cluster in our sample, Cluster 5. Cluster 5 is located in the heart of what Calzetti et al. (1997) refer to as the “starburst nucleus” of NGC 5253. Its measured UV slope is  $\beta = 0.06$  (after correction for the small amount of reddening from our own Galaxy), much redder than the expected slope of a 2 Myr old cluster,  $\beta \simeq -2.71$ . Using the starburst obscuration curve, the color excess implied by the difference between the slopes is  $E(B-V) = 0.42$ . The resulting intrinsic UV luminosity is  $L_{1500} = 1.0 \times 10^{38} \text{ ergs s}^{-1} \text{ \AA}^{-1}$ , taking the flux measured from the F170W image (to avoid slit losses) and assuming a distance of 3.33 Mpc. We use the number of ionizing photons reported by SB99 for a 2 Myr old cluster scaled

by  $L_{1500}^{obs}/L_{1500}^{model}$  and the transformations of Leitherer & Heckman (1995) to predict an extinction corrected  $H\alpha$  luminosity of  $L_{H\alpha} \simeq 3.6 \times 10^{39} \text{ erg s}^{-1}$ . This value is in reasonable agreement with the measured value of Calzetti et al. (1997), which is  $L_{H\alpha} \simeq 1.3 \times 10^{40} \text{ erg s}^{-1}$  after applying the same obscuration correction used above and taking into account the fact that the nebular gas is more reddened than the stellar flux by a factor of  $\sim 2.3$  (Calzetti et al. 2000)).

Unfortunately, this “dust scenario” is degenerate with a number of others, in the sense that multiple dust geometries can reproduce the observed quantities (UV slope and  $H\alpha$  flux), the only difference being the prediction of larger intrinsic luminosities, and hence the cluster masses. For instance, if we embed Cluster 5 in a dust cloud with  $A_V=35$  mag (Calzetti et al. 1997) with  $A_V \simeq 0.2$  of foreground dust, we recover the observed UV slope and  $H\alpha$  luminosity while predicting a cluster mass 10 times greater than that implied by the previous scenario. The dust cloud geometry can not be constrained by diagnostics at UV-optical wavelengths; for example, the maximum value of the color excess that is measurable from the Balmer decrement ( $H\alpha/H\beta$ ) in these cases is  $E(B-V) \lesssim 0.35$  (Calzetti 1997). Only by going to much longer wavelengths, such as the radio, can the degeneracy be broken (Beck et al. 1996; Calzetti 1997).

Cluster 5 has recently been mapped with the NRAO Very Large Array in the A configuration at wavelengths of 1.3 and 2 cm (Turner, Beck, & Ho 2000). The authors claim no optical counterpart for their source; however, the position of the dominant radio source is only  $1.17''$  distant from our pre-peak up coordinates for Cluster 5, which is within the error bars for absolute position measurements from *HST*. The radio source is partially optically thick at 2 cm, implying a Lyman continuum rate of  $3 \times 10^{52} \text{ s}^{-1}$  (Turner, Beck, & Ho 2000, corrected to 3.33 Mpc), which is about 3 times higher than that predicted on the basis of the observed dereddened  $H\alpha$  flux. We estimate a mass of  $4 \times 10^5 M_{\odot}$  for Cluster 5 by comparing the measured Lyman continuum rate with that reported by SB99 for a 2 Myr old  $10^6 M_{\odot}$  cluster with a Salpeter IMF extending from 1–100  $M_{\odot}$ . This value is a factor of  $\sim 10$  above the mass we derive solely on the basis of our UV measurements. However, it should be kept in mind that Cluster 5 is an extreme case: we expect luminosity and mass uncertainties to be substantially lower for most of the other clusters in our sample, since they are considerably less reddened.

Another factor which can contribute to underestimated masses for the stellar clusters is the adopted lower mass limit to the IMF. Direct measurements (Sirianni et al. 2000; Luhman et al. 2000) and morphological and dynamical information (Meurer et al. 1995; Ho & Filippenko 1996) favor a significant low-mass ( $<1 M_{\odot}$ ) population in stellar clusters. However, due to the observed flattening of the IMF at low masses, the total mass in stars should be similar to that derived using a Salpeter IMF extending down to  $1 M_{\odot}$ . If we take a more extreme assumption, for instance, if the IMF follows a Salpeter slope down to  $\sim 0.3 M_{\odot}$ , the clusters will be a factor  $\sim 1.6$  more massive than what is reported in Table 2.

### 5.2. Field

We investigated the diffuse light of NGC 5253 by creating spectra of three ‘field’ regions. We choose these regions such that they excluded any apparent clusters, but fell within the plateau of diffuse light (see Figure 2). The resultant one-dimensional field spectra have signal-to-noise values of 12 – 18, comparable the brightest clusters. The three field spectra are shown in Figure 4 and their measured properties are reported in Table 3. Since the three regions have similar spectral morphologies and amounts of reddening, we combine them into a single field spectrum which we use for all of our subsequent analysis.

The field spectrum does not show any evidence of the broad line profiles of N V, Si IV, and C IV which are characteristic of O-star winds. This is in sharp contrast to the spectra of the brightest clusters. The obvious disparity between the cluster and field spectra (see Figure 5) is clear evidence that the diffuse light is not simply reflected light from the clusters, but must originate in a UV bright field star population.

We devote our subsequent analysis to the nature of the field star population. What is immediately apparent from the weakness of the O-star wind features is that the field is deficient in the most massive stars. We consider whether this could be a statistical effect due to the small area and modest star formation rate of the region we are sampling. If we assume that the light in the field is the result of a continuous star formation episode, SB99 predicts that  $\sim 10$  O-stars should be present for a Salpeter IMF extending from 1 to  $100 M_{\odot}$ . (We have assumed a burst duration of 50 Myr, although the result is largely insensitive to this value.) The salient point is that a non-negligible number of O-stars is expected to be present. The fact that we do not see the spectral signatures of these high mass stars in our field spectrum indicates that either the IMF slope is steeper than Salpeter, the upper mass cut-off is lower than  $100 M_{\odot}$ , or that the stellar population has aged past  $\sim 10$  Myr. We create models to explore each of these scenarios.

We compare our various field models to the data using the same automated routines that we used for the clusters. However, we do not quote formal error bars on our best fits because the field spectrum has such high S/N that systematic errors dominate, as is evident in Figure 8. The probable sources of systematic error are discussed subsequently.

The power law slopes of models which are very deficient in massive stars are much shallower than our assumed value of -2.6 used for the clusters. In order not to bias our fits against these models, we rectify both the data and the models by fitting and dividing by the appropriate power law before comparison. Shallower intrinsic values of  $\beta$  imply less reddening in the data. This provides a useful constraint because models can not be redder than the extreme case of zero reddening for the field, which corresponds to  $\beta = -1.56$ , after correction for foreground Galactic reddening.

The first model we consider is the fiducial model that we use for the clusters: an instantaneous burst with a Salpeter IMF slope ( $\alpha = 2.35$ ) and an upper mass cut-off of  $M_{up} = 100 M_{\odot}$ . This model produces a best fit to the composite field spectrum at an age of 8 Myr. Younger

ages are strongly ruled out by the increasing strength of O-star wind lines. At ages older than about 8 Myr, the primary age discriminator becomes the strength of the B-star photospheric lines. However, the strength of these lines is expected to increase with metallicity, so the use of the solar metallicity B-star library could bias our fit towards younger ages. Thus, 8 Myr should be viewed as a lower bound to the age of the field. A strict upper bound of 45 Myr is set by the reddest model slope allowable, corresponding to the rather unlikely case of  $E(B-V) = 0$ . Ages of 8 - 18 Myr imply an  $E(B-V)$  value of  $\sim 0.17$ , in good agreement with the reddening of most of the clusters flanking the field regions. However, it is not implausible that the field could be less reddened than the stellar clusters.

The second model we consider is a continuous star formation model with a fixed age of 50 Myr, a Salpeter IMF slope, and variable upper mass cut-off. We test values of  $M_{up}$  of 10, 20, 30, 40, 50, and  $100 M_{\odot}$ , and find an upper mass cut-off of  $30 M_{\odot}$  is preferred. Higher upper mass cut-offs are strongly ruled out by the increasing presence of the O-star wind lines, particularly C IV. Values as low as  $10 M_{\odot}$  are unlikely because of the extreme strength of the B star photospheric lines (which are barely evident in the field spectrum). However, such models can not be conclusively eliminated because of the unknown impact of the solar metallicity B-star library on these features.

The third model we consider has continuous star formation with the age fixed at 50 Myr, the upper mass cut-off fixed at  $100 M_{\odot}$ , and a variable IMF slope. We examine values of  $\alpha = 2.35, 3, 3.5, 4,$  and  $5$ . The steepest slope we consider,  $\alpha = 5$ , corresponds to the ‘field star IMF’ derived by Massey et al. (1995) for the LMC and SMC. This model is ruled out a priori by the fact that it has an intrinsic slope of  $\beta = -0.89$ , far redder than the value measured for the field after correction for foreground reddening ( $\beta = -1.56$ ). The best fitting model,  $\alpha = 3.5$ , has a slope of  $\beta = -2.1$ , implying a very modest reddening of  $E(B-V) = 0.08$ . IMF slopes shallower than this are ruled out by the increasing width of the C IV stellar wind line.

The field spectrum is shown with each of the three model spectra overplotted in Figure 8 (a-c). None of the models provides a satisfactory fit. In each case, the continuum level of the data is above that of the models at wavelengths shortward of  $1270 \text{ \AA}$  and longward of  $1530 \text{ \AA}$ . In addition, photospheric lines like [S III]  $\lambda\lambda 1294, 1296, 1298 \text{ \AA}$  are grossly overpredicted. One consideration is that our subtraction of the geocoronal emission at Ly- $\alpha$  and [O I]  $\lambda 1302$  could be inducing errors in these regions of the spectrum. A residual emission feature is clearly observed in the field spectrum near  $1300 \text{ \AA}$ . However, other photospheric features such as Si II  $\lambda 1260$ , which are uncontaminated by geocoronal lines, are poorly matched with the models as well. It is also worth noting that the cluster data seem to be reasonably well fit in the regions surrounding the geocoronal lines, suggesting that sky subtraction is not a major source of error.

Another possibility is that the discrepancies between the data and the models are the result of a metallicity mismatch, as the stars with masses less than  $20 M_{\odot}$  (the predominant contributors to the continuum and photospheric lines in these models) have empirical spectra drawn

from the solar metallicity library. At solar metallicity, the broad wing of Lyman- $\alpha$  is more extended, and increased line blanketing is expected near 1550 Å, which could account for discrepancies in the continuum level. Also, photospheric lines are observed to be substantially weaker at LMC/SMC metallicity than at solar metallicity (Leitherer et al. 2001), consistent with what is seen in the field. However, until low metallicity B-stars spectra are added to the SB99 library, we can not be sure if this fully accounts for the discrepancy. An intriguing possibility is that the field spectrum might contain contributions from an older underlying stellar population. Adding a burst with an age of  $\sim 1$  Gyr to the models can eliminate the continuum mismatch problems at both ends; however, the already strong photospheric features become even stronger, and an unrealistically large stellar mass is implied. Until the metallicity issues are resolved, conclusions about an underlying older population are premature.

The parameters which provided the best fit for each of the three models are listed in Table 4 along with the measured power law slope of the model, and the implied reddening. The reduced  $\chi^2$  values of the best fits are also given for reference. We do not use these values to discriminate among the models, since the differences are relatively minor and the overall quality of the fits is not high. We consider the plausibility of each of the models further in §6.2.

## 6. DISCUSSION

### 6.1. *The Stellar Clusters: Ages and Masses*

The eight clusters subtended by our slit all have ages below  $\sim 10$  Myr, with three having ages  $< 3$  Myr, for a Salpeter IMF in the range 1–100  $M_{\odot}$ . Among the three youngest is Cluster 5, the primary target of our STIS observations, whose very young age is in agreement with that inferred by Calzetti et al. (1997) based on the large observed equivalent width of the H $\alpha$  emission line ( $EW(H\alpha)=1650$  Å).

Notably young are Clusters 2 and 3, with ages 8 Myr and 3 Myr, respectively. For these two clusters, age estimates based on colors give values of  $\sim 60$  Myr and  $\sim 30$  Myr, respectively (Calzetti et al. 1997), much larger than what is inferred from UV spectroscopy. Age determinations based on colors alone are indeed bound to be relatively uncertain unless additional constraints (e.g., H $\alpha$  emission) are available. For instance, consider Cluster 2: the difference in  $B-V$  color between a 60 and a 8 Myr old instantaneous burst is only  $\sim 0.18$  mag. The narrowness of this range makes accurate reddening corrections imperative. Calzetti et al. (1997) deredden their observed colors based on the ratio of H $\alpha$  to H $\beta$ ; however the measured equivalent widths are very small ( $< 4$  Å) and therefore bound to be uncertain. After correction for galactic foreground reddening and underlying stellar absorption, they find zero magnitudes of foreground attenuation between H $\alpha$  and H $\beta$ . By contrast, the reddening derived from our UV spectroscopy is  $E(B-V) = 0.16$ , very nearly what is needed to bring the broad-band color age estimate into line. Similar results are found for Cluster 3, although the  $B-V$  color difference between the two age estimates is greater ( $\sim 0.3$ ) and can not be entirely reconciled by applying our reddening correction. Additional corroboration for the young

ages of Clusters 2 and 3 comes from an analysis of the soft X-ray emission near the center of NGC 5253 (Strickland & Stevens 1999). The two clusters appear to be located within a superbubble of expanding hot gas. Energy limitations constrain the age of the superbubble to be  $\lesssim 10$  Myr (Strickland & Stevens 1999), in better agreement with the age estimates from UV spectroscopy.

The measured and derived properties of the clusters are summarized in Tables 1 and 2. The ages of the clusters show no particular spatial correlation (which could indicate propagating star formation.) Their half-light radii span a wide range of values (0.6 – 2.4 pc), but visual examination of the profiles suggests that the largest clusters are an unresolved blend of smaller ones. The clusters display varying amounts of reddening, ranging from  $E(B-V) = 0.42 - 0.05$ . The reddening values show a broad spatial correlation; that is, clusters which are physically close show similar amounts of reddening. The extinction-corrected 1500 Å luminosities are in the range  $L_{1500} \sim 10^{35} - 10^{38}$  ergs  $s^{-1}$  Å $^{-1}$  for the eight clusters, implying masses in the  $10^2 - 10^4 M_{\odot}$  range, for a low-end IMF mass of 1  $M_{\odot}$ . However, both luminosities and masses listed can generally be considered lower limits to the actual values, as discussed in §5.1. We note that the lowest mass clusters ( $10^3 M_{\odot}$  or less) might be subject to strong stochastic effects since only a handful of O-stars are expected to be present for a Salpeter IMF. These effects could potentially bias our age and mass determinations for Clusters 9, 10, and 11.

### 6.2. *The Stellar Field: The Final Stop for the Evolution of Clusters?*

The UV emission from the field regions surrounding the clusters has a clearly stellar origin and is not due to reflected light from the clusters themselves, since, as already mentioned in §5.2, the spectral features of clusters and field are notably different. In contrast to the clusters spectrum, the field spectrum lacks the strong O-star wind lines of N V, Si IV, and C IV which are signatures of the most massive stars. We stress that this deficiency is not an artifact of undersampling of the field, as our field spectrum contains a considerable amount of light. In fact, the field has a flux nearly equivalent to the integrated cluster spectrum, which contains over  $6 \times 10^4 M_{\odot}$  of stars. A similar discrepancy between the cluster and field population has been observed in the starburst galaxy NGC 1569. Using WFPC2 photometry, Greggio et al. (1998) find that the stellar population of NGC 1569 is composed of recently formed super star clusters and resolved field stars with ages greater than 10 Myr.

In order to understand why the field might be deficient in massive stars we have compared the field spectrum of NGC 5253 to three different families of model spectra. The first is an instantaneous burst model with a Salpeter IMF in the 1–100  $M_{\odot}$  range. Our best fit model has an age of 8 Myr, although this should be considered a lower limit for the reasons discussed in §5.2. While this model provides a reasonable fit to the data, we rule it out on physical grounds: our field regions are spatially extended ( $\sim 80$  pc) and therefore unlikely to be forming stars in an instantaneous burst. The subsequent models we consider have continuous star formation which is probably more appropriate



given the galaxy's  $\sim 10$  Myr crossing time.

Since the age of the burst is largely irrelevant in continuous models, we allow the free parameters to be the slope and upper mass cut-off of the IMF. Our second model uses a fixed Salpeter slope and a variable upper mass cut-off. A reasonable fit is produced for an upper mass cut-off of  $\sim 30 M_{\odot}$ . The third model fixes the upper mass cut-off at 100 and allows the IMF slope to vary. The best fit is achieved by a value of  $\alpha = 3.5$ , which is steeper than Salpeter, but shallower than the  $\alpha \sim 5$  value found by Massey et al. (1995) for the stellar field of the Magellanic clouds. An IMF slope of  $\alpha = 5$  is strongly ruled out by the observed blue color of the field's UV continuum (although it might be argued that our definition of the 'field' is not as rigorous as Massey's.) We note that our fits are sensitive to stars with masses  $\gtrsim 20 M_{\odot}$  which is comparable to the stellar mass range  $\sim 15\text{--}60 M_{\odot}$  sampled by Massey et al. (1995).

The basic result is that the field of NGC 5253 is generally lacking very massive stars, either because of aging or because very massive stars do not form in large numbers. Meurer et al. (1995) found that the field accounts for a significant fraction of the UV light from starbursts, between 50% and 80%, and proposed that the field is the outcome of diffuse star formation, a mode different from the one which produces stellar clusters. If the hypothesis that two modes of star formation exist in starbursts is correct, then our observations show that the two modes produce drastically different IMFs: a 'regular' Salpeter IMF up to  $\sim 100 M_{\odot}$  in clusters, and a massive-star-deficient IMF in the field.

A scenario other than bi-modal star formation can be suggested to explain the properties of the stellar field. The eight clusters along our STIS slit are all younger than  $\sim 10$  Myr; the other three bright clusters in the center of NGC 5253 are younger than  $\sim 20$  Myr, although for two of the clusters ages have been derived from photometry alone and can therefore be fairly uncertain (Kobulnicky et al. 1997; Schaerer et al. 1997; Calzetti et al. 1997). If the clusters along our slit are representative of the general cluster population in the center of NGC 5253, we can conclude that the field appears generally older than the clusters or as old as the oldest among them. The field thus contains stars at a more advanced evolutionary stage than the clusters. One way to obtain such a population mix is to hypothesize that stellar clusters dissolve over timescales of  $\sim 10\text{--}20$  Myr and their surviving stars disperse into the field. Thus, there is only one star formation mode: stars form in clusters and a fraction of them continue their life in the field.

To test this hypothesis, we have constructed a model for the field by subtracting a 10 Myr constant star formation population from a 100 Myr constant star formation population. Star formation has been going on for a while in the center of NGC 5253 (e.g., Calzetti et al. 1997), and if clusters dissolve over a timescale of  $\sim 10$  Myr, the field will consist of stars with ages between  $\sim 10$  Myr and the maximum age of the star formation episode, which we take to be 100 Myr, although the resulting UV spectrum is largely insensitive to this value. Figure 8 d) compares the field to the 100 – 10 Myr model spectrum. The similarity between this model spectrum and the other models shown in Figure

8 is not surprising: the UV spectrum of the 100 – 10 Myr model is dominated by its youngest, most luminous contributors, i.e., stars with ages  $\sim 10$  Myr which have just come out of dissolving stellar clusters.

One prediction of the 100 – 10 Myr model is that about 40% of the UV light at  $1500 \text{ \AA}$  is in the field. This fraction becomes slightly higher as one goes to longer wavelengths, for instance, at  $2200 \text{ \AA}$  (the wavelength of the Meurer et al. (1995) study) the fraction becomes 45%. However, this value is still somewhat below the 50–80% value derived for nearby starbursts (Buat et al. 1994; Meurer et al. 1995; Maoz et al. 1996). Pushing the dissolution timescale to an age as young as 6 Myr, brings the fraction of light in the field to  $>50\%$ . However, the differences between the measured and predicted fraction of light in the field may simply reflect the observational difficulty of disentangling small clusters from the field population.

Star clusters are known to dynamically evolve, with a number of mechanisms contributing to stellar depletion eventual cluster dissolution. However, the dissolution timescales implied by our model for NGC 5253 are very short. We consider the feasibility of these timescales using the model results of Kim, Morris & Lee (1999). Kim, Morris & Lee (1999) calculated the evaporation timescales for compact (half-mass radius  $\leq 1$  pc) stellar clusters near the center of the Milky Way, including stellar evolution among the ingredients. With the possible exception of 5, our clusters appear fairly compact, with half-light radii  $< 2$  pc; we assume that the half-light radii are a reasonable approximation of the half-mass radii, although mass segregation may have already acted on the oldest clusters to make the first radius smaller than the second. The environment surrounding our clusters is also quite different from that of the Milky Way. NGC 5253 has about 100 times less baryonic mass than the Galaxy, spread over about 20 times less volume (adopting flattened mass distributions for both galaxies, with similar scale heights); this implies that the central density in NGC 5253 is about 5 times lower than the central density in the Milky Way. Kim, Morris & Lee (1999) identify the tidal radius as one of the crucial parameters which determines the evaporation timescale of the stellar clusters; in NGC 5253 the stellar clusters have tidal radii about 70% bigger than in the Milky Way, for constant cluster mass, and, thus, evaporation timescales about 2.2 times longer. A  $5 \times 10^3 M_{\odot}$  cluster placed 100 pc away from the dynamical center of NGC 5253 will evaporate in  $\sim 15$  Myr for a 1–150  $M_{\odot}$  Salpeter IMF or in  $\sim 25$  Myr for a 0.1–150  $M_{\odot}$  Salpeter IMF. We are therefore in the expected ballpark timescale for the less massive among our clusters to agree with the dissolving clusters scenario; heavier clusters, like 2, will have lifetimes in the range of 50–100 Myr and will not contribute significantly to the UV emission of the field. The most massive of our clusters, Cluster 5, has a relaxation time of 400 Myr for a 1–150  $M_{\odot}$  Salpeter IMF, and is potentially bound if the IMF extends to lower stellar masses.

A final consideration is the validity of our definitions of 'cluster' and 'field'. The first issue of concern is that some of the less massive objects which we have defined as clusters may simply be random superpositions of a few field O-stars. In this scenario our finding of an massive star

deficient field population would be merely circular logic since we would have selectively eliminated many of the O-stars from the field. The brightness of Clusters 9, 10, and 11, while lower limits, could be consistent with being one to a few O-stars or B supergiants. However, all of these clusters are well resolved and have relatively smooth spatial profiles. (Cluster 8, which may include a bright point source, was previously discussed in § 5.1.) An additional check is performed by adding the light from Clusters 8, 9, 10, and 11 to our field spectrum. These four clusters contribute about 20% of the total field light, but produce a negligible difference in the integrated spectrum. Thus, we can be relatively secure that our choice of clusters is not robbing the field of O-stars.

The other issue of concern is the converse: that what we call the field may in fact include a number of faint unresolved clusters. Taking the flux of our faintest cluster as our detection limit, we find that a  $10^4 M_{\odot}$  cluster with an  $E(B-V)$  of 0.2 would be detectable with an age as old as 50 Myr, while a  $10^3 M_{\odot}$  cluster with a similar amount of reddening would only be seen at ages less than 15 Myr. Clusters with masses less than  $10^3 M_{\odot}$  probably do not contribute much UV light since they are unlikely to contain many very massive stars due to statistical effects. Thus, clusters which are both relatively old and not very massive could contribute somewhat to our field population. However, such light-weight clusters would be subject to a number of destruction mechanisms, and would tend to dissolve on timescales shorter than those discussed above (Kim, Morris & Lee 1999). Most importantly, the addition of faded clusters to the field would not alter the basic notion that there is only one ‘mode’ of star formation.

### 6.3. High Redshift Galaxies

The differences seen in the spectra of the field and clusters of NGC 5253 have potentially important implications for restframe UV observations of high redshift galaxies. Because of the small angular sizes of high redshift objects, the entire star-forming region is typically observed, with no discrimination between clusters and field. Since the field’s UV light may represent between 50% and 80% of the UV output from a starburst galaxy (Buat et al. 1994; Meurer et al. 1995; Maoz et al. 1996), the common tendency to compare spatially integrated spectra of distant galaxies with the UV spectra of local stellar clusters neglects the important contribution of the field. To quantify this statement, we have created two ‘integrated’ spectra, the first combining a 50% ‘cluster’ spectrum with 50% ‘field’ spectrum, and the second with a 20%–80% cluster–field mix (Figure 9). The ‘cluster’ spectrum is the unweighted sum of the eight clusters along our slit prior to dereddening. The 50–50 and 20–80 template spectra are available for download from <http://www.stsci.edu/starburst/templ.html>.

The spectral features of the 50–50 ‘integrated’ spectrum closely resemble those of a continuous starburst with a standard Salpeter IMF extending up to  $100 M_{\odot}$ . The 20–80 integrated spectrum has weaker wind lines than the 50–50 mix, and may be more appropriate to populations with declining star formation rates. In both cases the stellar wind lines, most notably C IV  $\lambda 1550$ , are substantially weaker than in a pure young population. Thus, the gen-

erally observed weakness or even absence of stellar wind lines in high- $z$  galaxies (e.g., Lowenthal et al. 1997) may not be entirely a metallicity effect, but rather a result of time-extended star-forming episodes.

The utility of our template spectra for comparisons with high redshift galaxies is illustrated in Figure 10, where we compare our 50% cluster–50% field spectrum to the spectrum of the gravitationally lensed  $z = 2.73$  starburst galaxy, MS 1512-cB58 (Pettini et al. 2000). cB58 appears to be a relatively typical  $L^*$  Lyman break galaxy, with  $Z \approx 1/3 Z_{\odot}$  (Teplitz et al. 2000). Our empirical template provides an exceptionally good fit overall to the stellar features, particularly to the stellar wind lines. The widths of the interstellar features appear to be fairly well matched, but it must be kept in mind that the interstellar features of the NGC 5253 template spectrum are artificially broadened by blending with intervening Milky Way absorption features. The intrinsically broader and deeper interstellar features of cB58 are probably a result of the larger covering factor of the gas, and the hydrodynamical consequences of the galaxy’s high star formation rate. Thanks to the exceptional S/N of both cB58 ( $\sim 40$ ) and our template spectrum ( $\sim 30$ ), Figure 10 provides one of the best examples to date of the striking similarity between the spectral morphology of a high redshift star-forming galaxy and a local starburst.

## 7. SUMMARY & CONCLUSIONS

We have obtained a STIS longslit UV spectrum of the central star forming region of the dwarf starburst galaxy NGC 5253. We extracted spectra of 8 clusters and three field regions along the slit, and compared these spectra to the STARBURST99 stellar evolutionary synthesis models. The clusters are well fit by instantaneous burst models with a standard Salpeter IMF extending from 1– $100 M_{\odot}$ . We derive ages for the clusters in the range 1–10 Myr and masses in the range  $10^2$ – $10^4 M_{\odot}$ , although the latter are probably underestimated by factors of a few.

The spectral features of the field and the brightest clusters exhibit pronounced differences, clear proof that the diffuse UV light is not simply reflected cluster light. The main difference is that the field of NGC 5253 is found to be lacking in the most massive stars, either as a consequence of aging or because massive stars are not forming in the field in large numbers. One possibility is that star formation in starbursts is bimodal, with compact clusters forming stars with a standard Salpeter IMF extending up to  $100 M_{\odot}$ , and more diffuse star formation occurring with a massive-star deficient IMF. We suggest an alternate hypothesis which requires only one ‘mode’ of star formation. In this scenario, stellar clusters form continuously and dissolve on  $\sim 10$  Myr time scales, dispersing their remaining stars into the field. We find this hypothesis to be consistent with the evaporation timescales that we derive for the majority of our clusters.

Our dissolving clusters scenario suggests that continuous star formation models with a standard Salpeter IMF in the range 1– $100 M_{\odot}$  should be appropriate for the integrated spectra of high- $z$  galaxies, which will contain both young clusters and their dissolved by-products, field stars. The commonly observed absence of very broad O-star wind lines in high redshift galaxies may indicate that we are

observing star formation episodes of sufficient duration to populate the field with substantial numbers of older stars. Care must be taken when comparing high resolution rest-frame UV spectra of distant galaxies to local starburst templates because the presently available template spectra are primarily of individual star clusters. We have constructed a 50% cluster–50% field and a 20% cluster–80% field spectrum of NGC 5253 which we present as new benchmarks for comparison with spectra of high- $z$  galaxies.

The authors would like to thank Gerhardt Meurer for insightful and stimulating discussions which helped shape this paper; Duilia de Mello for her expert advice about B star lines; and Max Pettini and Chuck Steidel for contributing the spectrum of MS 1512-cB58. We also wish to thank our anonymous referee for his or her helpful comments. We are grateful for support we received from NASA through Grant No. GO-08232.01.97A from the Space Telescope Science Institute which is operated by the Association of Universities for Research in Astronomy, Inc. for NASA under contract NAS5-26555.

## REFERENCES

- Adelberger, K. L., & Steidel, C. C. 2000, *ApJ*, 544, 218
- Beck, S. C., Turner, J. L., Ho, P. T. P., Lacy, J. H., & Kelly, D. M. 1996, *ApJ*, 457, 610
- Buat, V., Vuillemin, A., Burgarella, D., Milliard, B., & Donas, J. 1994, *A&A*, 281, 666
- Burstein, D., & Heiles, C. 1982, *AJ*, 87, 1165
- Caldwell, N., & Phillips, M. M. 1989, *ApJ*, 338, 789
- Calzetti, D. 1997, *AJ*, 113, 162
- Calzetti, D., Conzelmann, C. J., Gallagher, J. S., & Kinney, A. L. 1999, *AJ*, 118, 797
- Calzetti, D., Kinney, A. L., & Storchi-Bergmann, T. 1994, *ApJ*, 429, 582
- Calzetti, D., Meurer, G. R., Bohlin, R. C., Garnett, D. R., Kinney, A. L., Leitherer, C., & Storchi-Bergmann, T. 1997, *AJ*, 114, 1834
- Calzetti, D., Armus, L., Bohlin, R. C., Kinney, A. L., Koornneef, J., & Storchi-Bergmann, T. 2000, *ApJ*, 533, 682
- Campbell, A. W., & Terlevich, R. 1984, *MNRAS*, 211, 15
- Campbell, A., Terlevich, R., & Melnick, J. 1986, *MNRAS*, 223, 811
- Cardelli, J. A., Clayton, G. C., & Mathis, J. S. 1989, *ApJ*, 345, 245
- Garcia-Vargas, M. L., Bressan, A., & Diaz, A. I. 1995, *A&AS*, 112, 13
- Garmany, C. D., & Conti, P. S. 1985, *ApJ*, 293, 407
- Gibson, B. K., et al., *ApJ*, 529, 723
- Greggio, L., Tosi, M., Clampin, M., de Marchi, G., Leitherer, C., Nota, A., & Sirianni, M. 1998, *ApJ*, 504, 725
- Heckman, T. M., Robert, C., Leitherer, C., Garnett, D. R., & van der Rydt, F. 1998, *ApJ*, 503, 646
- Ho, L. C., & Filippenko, A. V. 1996, *ApJ*, 472, 600
- Hunter, D. A., O'Neil, E. J., Lynds, R., Shaya, E. J., Groth, E. J., & Holtzman, J. A. 1996, *ApJ*, 459, L27
- Kennicutt, R. C., et al., *ApJ*, 498, 181
- Kim, S. S., Morris, M., & Lee, H. M. 1999, *ApJ*, 525, 228
- Kobulnicky, H. A., Skillman, E. D., Roy, J., Walsh, J. R., & Rosa, M. R. 1997, *ApJ*, 477, 679
- Kobulnicky, H. A., Kennicutt, R. C., & Pizagno, J. L. 1999, *ApJ*, 514, 544
- Leitherer, C., & Heckman, T. M. 1995, *ApJS*, 96, 9
- Leitherer, C., et al., 1999, *ApJS*, 123, 3
- Leitherer, C., Leão, J. R. S., Heckman, T. M., Lennon, D. J., Pettini, M., & Robert, C. 2001, *ApJ*, in press
- Lowenthal, J. D., et al., 1997, *ApJ*, 481, 673
- Luhman, K. L., Rieke, G. H., Young, E. T., Cotera, A. S., Chen, H., Rieke, M. J., Schneider, G., & Thompson, R. I. 2000, *ApJ*, 540, 1016
- Martin, C. L., & Kennicutt, R. C. 1995, *ApJ*, 447, 171
- Massey, P., & Hunter, D. A. 1998, *ApJ*, 493, 180
- Massey, P., Lang, C. C., Degioia-Eastwood, K., & Garmany, C. D. 1995, *ApJ*, 438, 188
- Massey, P., Johnson, K. E., and Degioia-Eastwood, K. 1995, *ApJ*, 454, 151
- Massey, P. 1998, *ASP Conf. Ser. 142: The Stellar Initial Mass Function (38th Herstmonceux Conference)*, 17
- de Mello, D. F., Leitherer, C., & Heckman, T. M. 2000, *ApJ*, 530, 251
- Meurer, G. R., Heckman, T. M., & Calzetti, D. 1999, *ApJ*, 521, 64
- Meurer, G. R., Heckman, T. M., Lehnert, M. D., Leitherer, C., & Lowenthal, J. 1997, *AJ*, 114, 54
- Meurer, G. R., Heckman, T. M., Leitherer, C., Kinney, A., Robert, C., & Garnett, D. R. 1995, *AJ*, 110, 2665
- Maoz, D., Barth, A. J., Sternberg, A., Filippenko, A. V., Ho, L. C., Macchetto, F. D., Rix, H. -W., & Schneider, D. P. 1996, *AJ*, 111, 2248
- Pettini, M., Steidel, C. C., Adelberger, K. L., Dickinson, M., & Giavalisco, M. 2000, *ApJ*, 528, 96
- Puls, J., et al. 1996, *A&A*, 305, 171
- Robert, C., Leitherer, C., & Heckman, T. M. 1993, *ApJ*, 418, 749
- Rogstad, D. H., Lockart, I. A., and Wright, M. C. H. 1974, *ApJ*, 193, 309
- Sandage, A., & Brucato, R. 1979, *AJ*, 84, 472
- Scalo, J. 1998, *ASP Conf. Ser. 142: The Stellar Initial Mass Function (38th Herstmonceux Conference)*, 201
- Schaerer, D., Contini, T., Kunth, D., & Meynet, G. 1997, *ApJ*, 481, L75
- Sirianni, M., Nota, A., Leitherer, C., De Marchi, G., & Clampin, M. 2000, *ApJ*, 533, 203
- Stasinska, G., & Leitherer, C. 1996, *ApJS*, 107, 661
- Steidel, C. C., Giavalisco, M., Pettini, M., Dickinson, M., & Adelberger, K. L. 1996, *ApJ*, 462, L17
- Steidel, C. C., Adelberger, K. L., Giavalisco, M., Dickinson, M., & Pettini, M. 1999, *ApJ*, 519, 1
- Strickland, D. K., & Stevens, I. R. 1999, *MNRAS*, 306, 43
- Teplitz, H. I., et al., *ApJ*, 533, L65
- Turner, J. L., Beck, S. C., & Ho, P. T. P. 2000, *ApJ*, 532, L109
- Turner, J. L., Ho, P. T. P., & Beck, S. C. 1998, *AJ*, 116, 1212
- Walborn, N. R., Lennon, D. J., Haser, S. M., Kudritzki, R., & Voels, S. A. 1995, *PASP*, 107, 104
- Walborn, N. R., Lennon, D. J., Heap, S. R., Lindler, D. J., Smith, L. J., Evans, C. J., & Parker, J. W. 2000, *PASP*, 112, 1243
- Walsh, J. R., & Roy, J. 1987, *ApJ*, 319, L57
- Walsh, J. R., & Roy, J. 1989, *MNRAS*, 239, 297
- Webster, B. L., & Smith, M. G. 1983, *MNRAS*, 204, 743

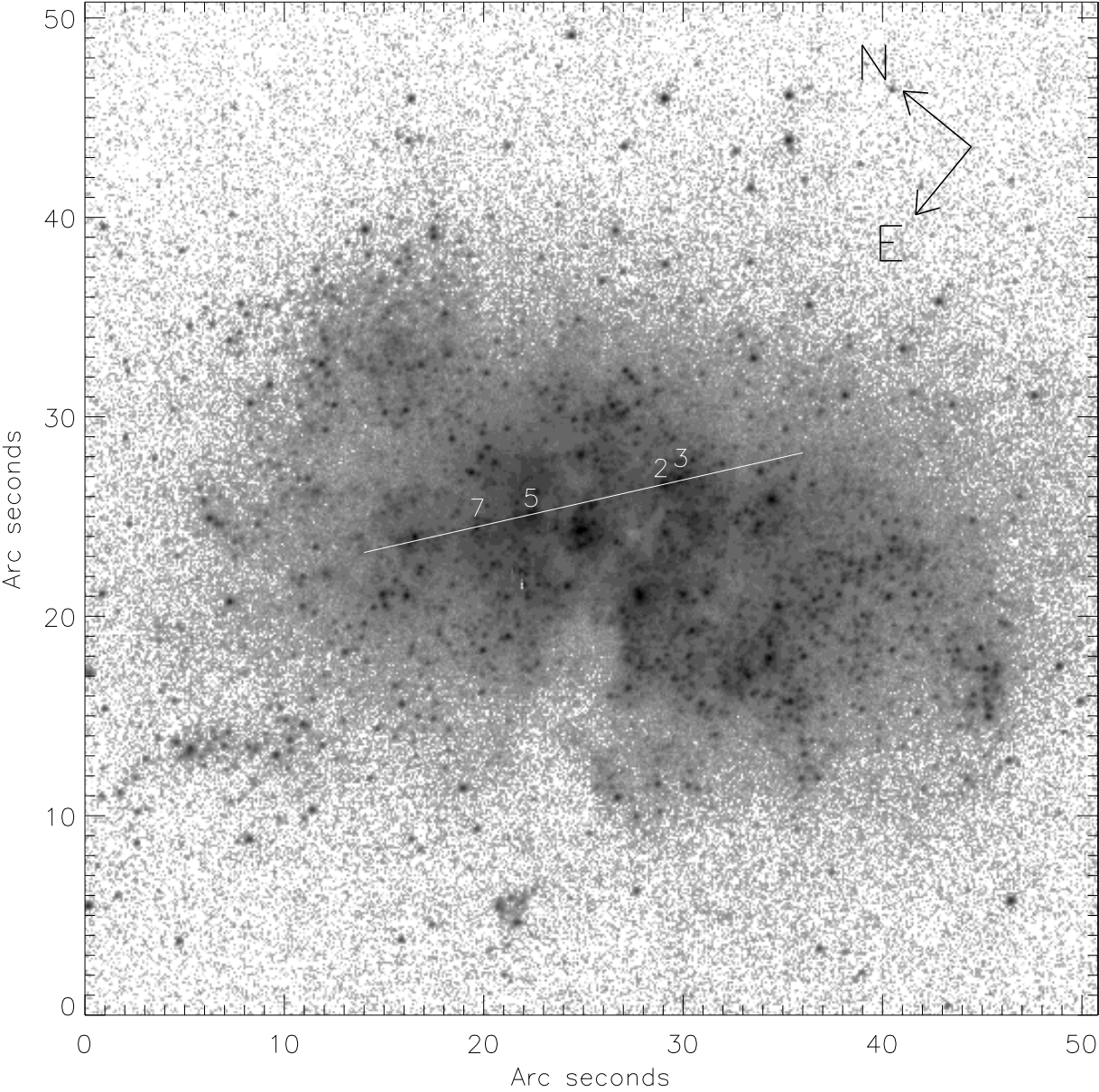


FIG. 1.— A *Hubble Space Telescope* WFPC2 image of NGC 5253 in the F255W filter. The approximate placement of the slit is shown, and Clusters 2, 3, 5, and 7 are labeled for reference. One arcsecond corresponds to  $\sim 16$  pc.

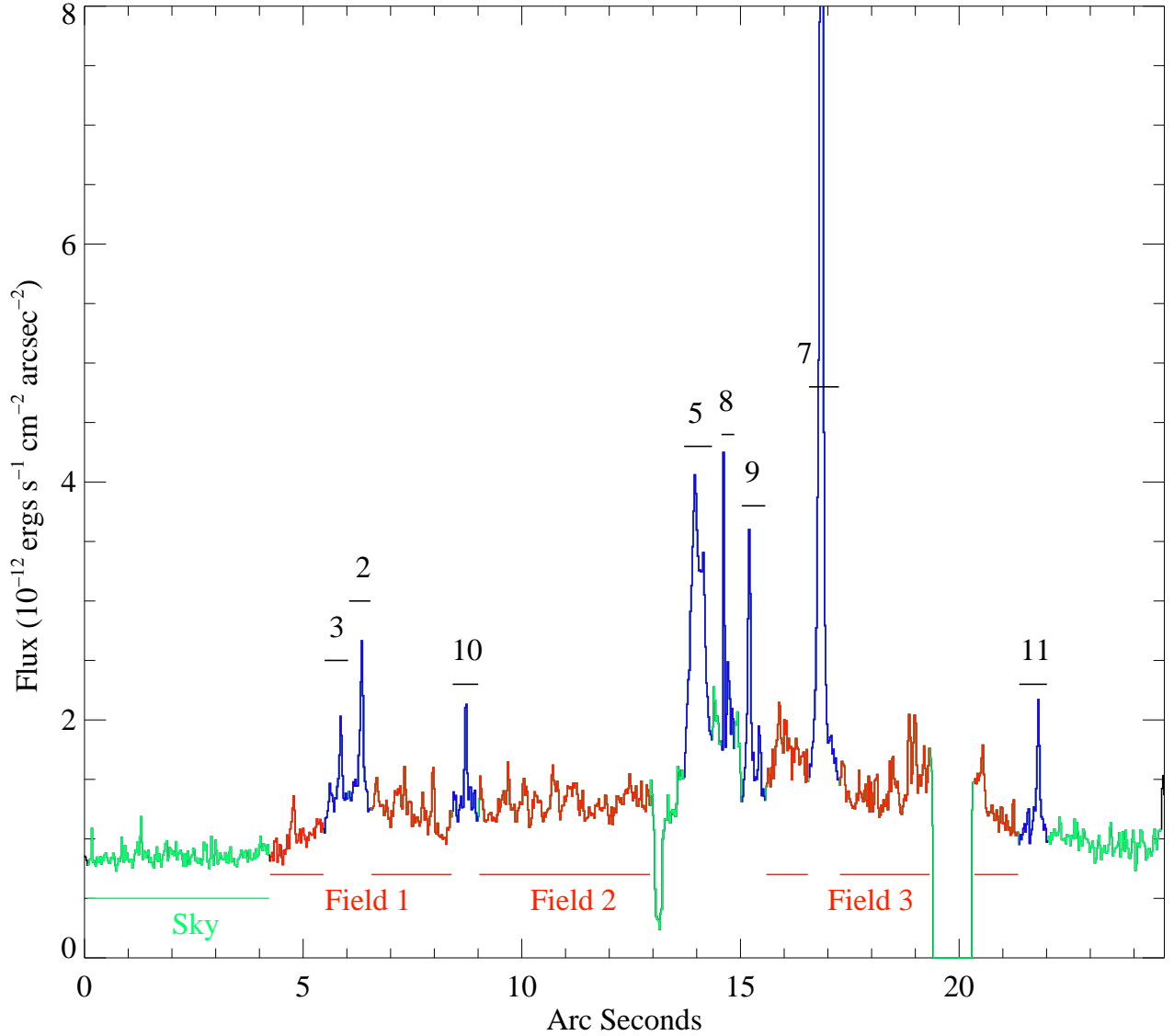


FIG. 2.— The integrated 1150 – 1710 Å flux as a function of position along the slit. Note the plateau of diffuse light extending from roughly 4 – 22'' along the slit. The regions defined as clusters are shown in blue and labeled 2 – 11, in accordance with the convention of Calzetti et al. (1997). The three regions which we take to be the field are shown in dark red. The portion of the spectrum used for the subtraction of the geocoronal lines is labeled “sky”. Horizontal bars indicate the extent of the extraction windows. The areas where the spectrum falls to zero are artifacts of the STIS occulting bar and repeller wire.

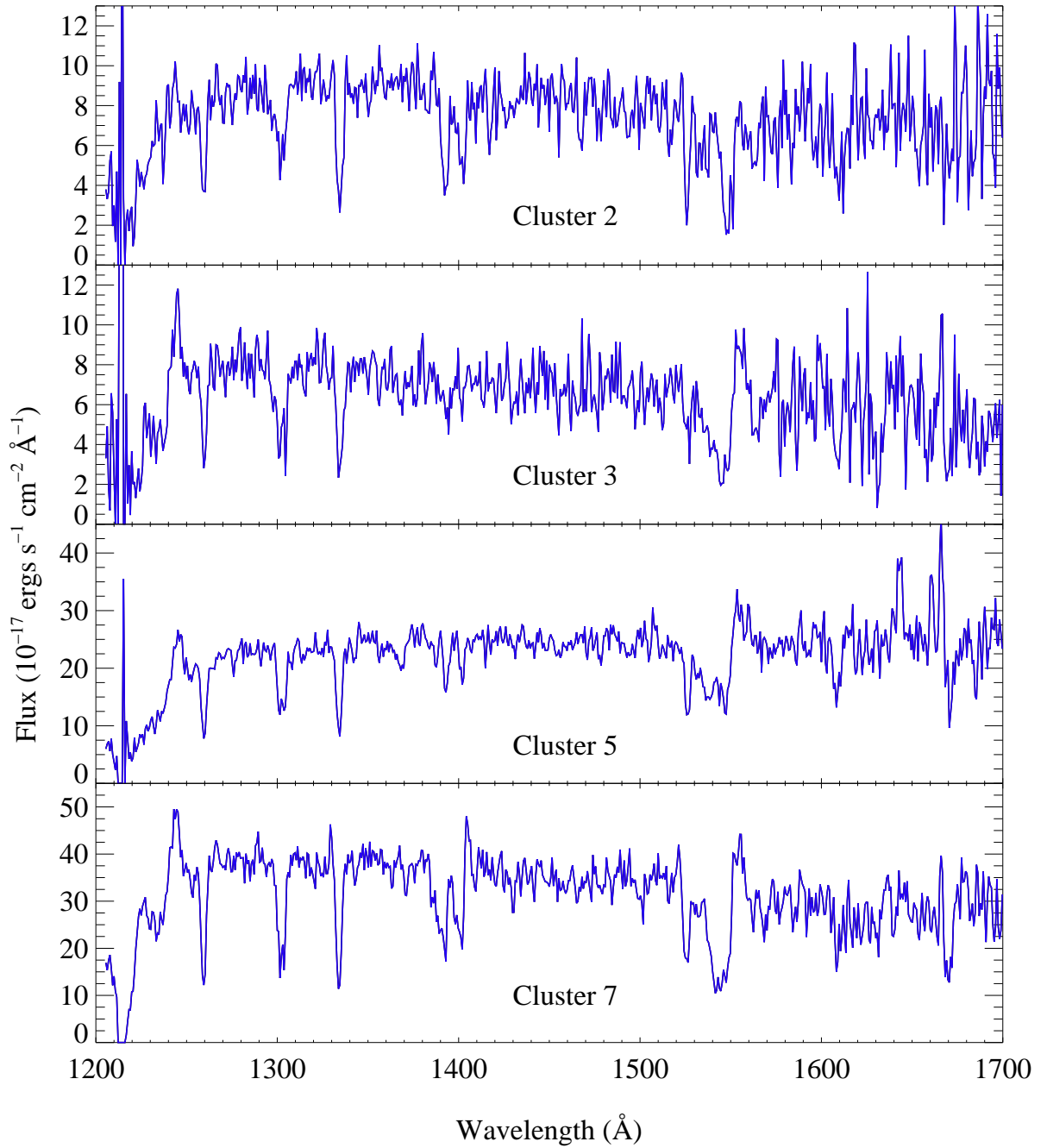


FIG. 3.— Spectra of the four brightest clusters 2, 3, 5, and 7 are shown for comparison. These data have not been corrected for reddening or slit losses.

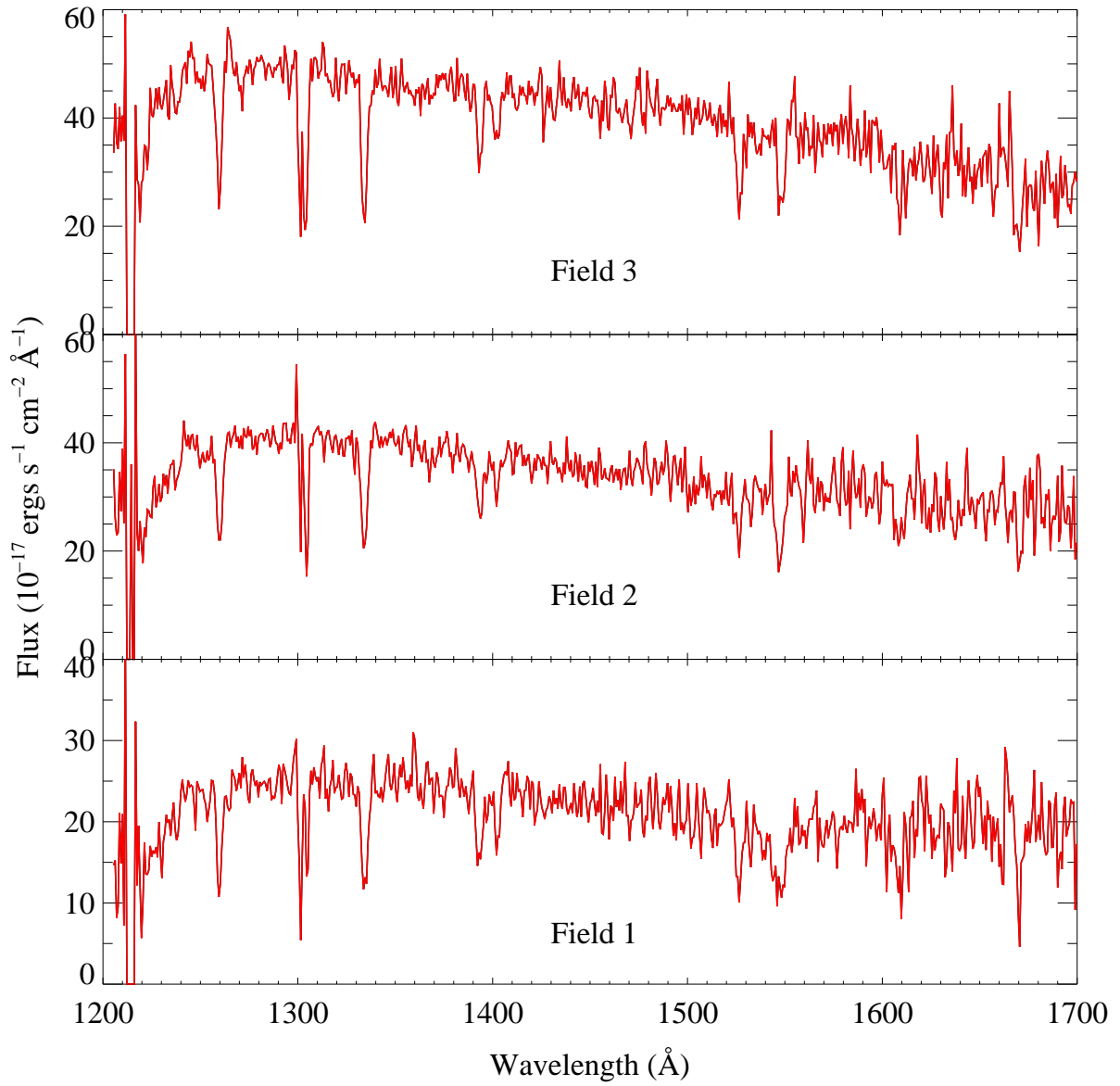


FIG. 4.— Spectra of the three field regions are shown for comparison. The data have not been corrected for reddening. Imperfect subtraction of the geocoronal Ly- $\alpha$  and O I  $\lambda$ 1302 lines produces the residual spikes seen near Ly- $\alpha$  and the spurious emission feature near 1300  $\text{\AA}$  in Field 2.



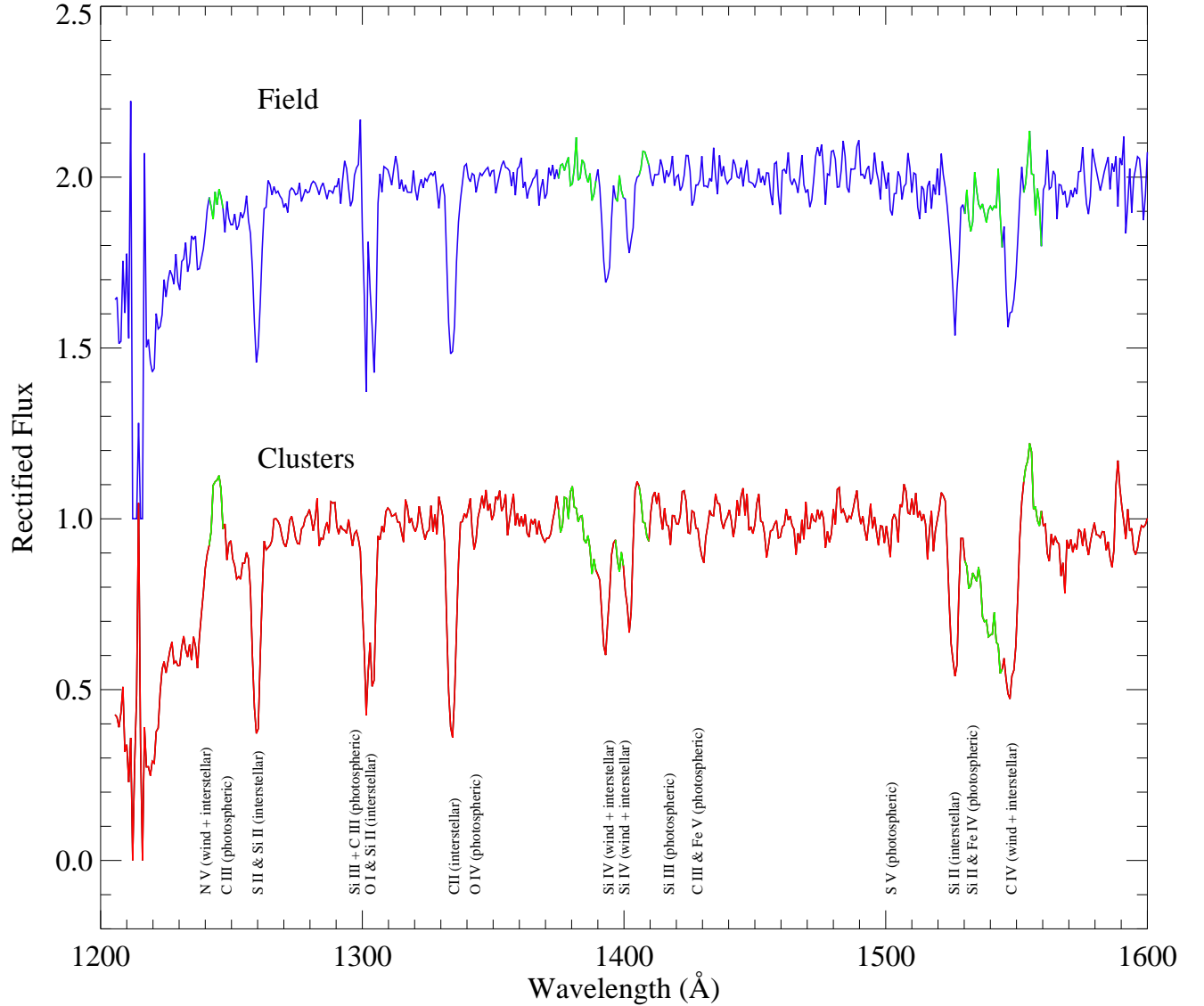


FIG. 5.— The rectified spectrum of the field (top) is shown with the combined spectrum of the clusters (bottom) for comparison. The cluster spectrum shows the clear signatures of O-stars in the the broad stellar wind P-Cygni features of N V  $\lambda 1240$ , Si IV  $\lambda 1400$ , and C IV  $\lambda 1550$  (highlighted in green.) The corresponding features are greatly reduced in the B-star dominated field spectrum. A number of stellar wind and photospheric features are labeled as are the prominent interstellar lines, which are a blend of the intrinsic starburst lines and foreground Milky Way absorption. We note that the spikes seen near Ly- $\alpha$  and the emission feature seen near 1300  $\text{\AA}$  in the field spectrum are residuals from the geocoronal line subtraction. The regions highlighted in grey are the stellar wind lines with their interstellar cores removed. These regions are especially sensitive to the age/stellar composition of the population and are heavily weighted in determining the best fit of evolutionary synthesis model spectra to the data.

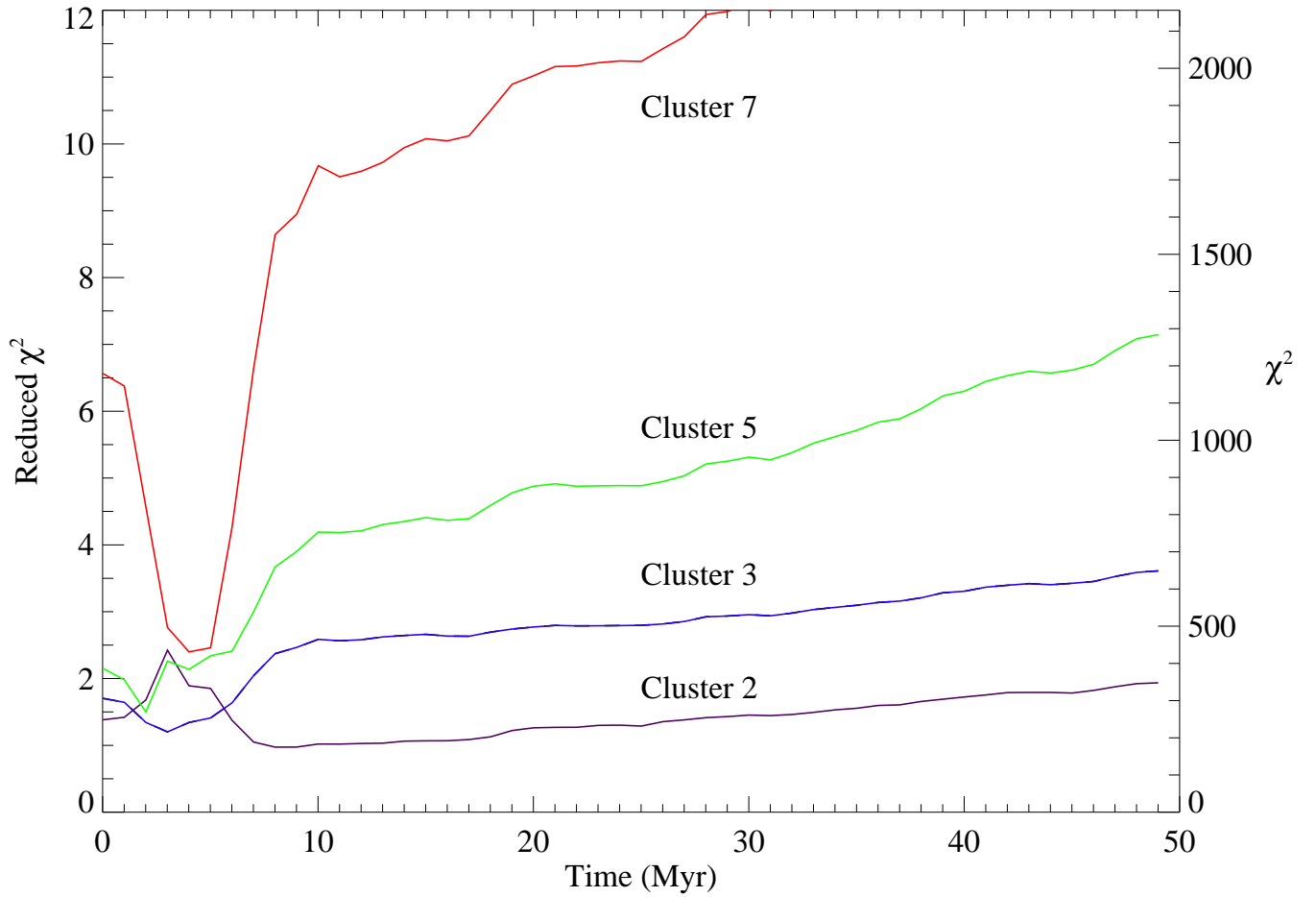


FIG. 6.— The  $\chi^2$  evolution of an instantaneous burst model fit to Clusters 2, 3, 5, and 7 is shown. The shape of the  $\chi^2$  provides information about the robustness of the fit. Cluster 5, for example, has an age which is tightly constrained to be near 2 Myr by its steep  $\chi^2$  slope on either side of minimum. In contrast, the evolution of the  $\chi^2$  for Cluster 2 is relatively flat after  $\sim 8$  Myr, indicating a large uncertainty on the upper bound of its age.

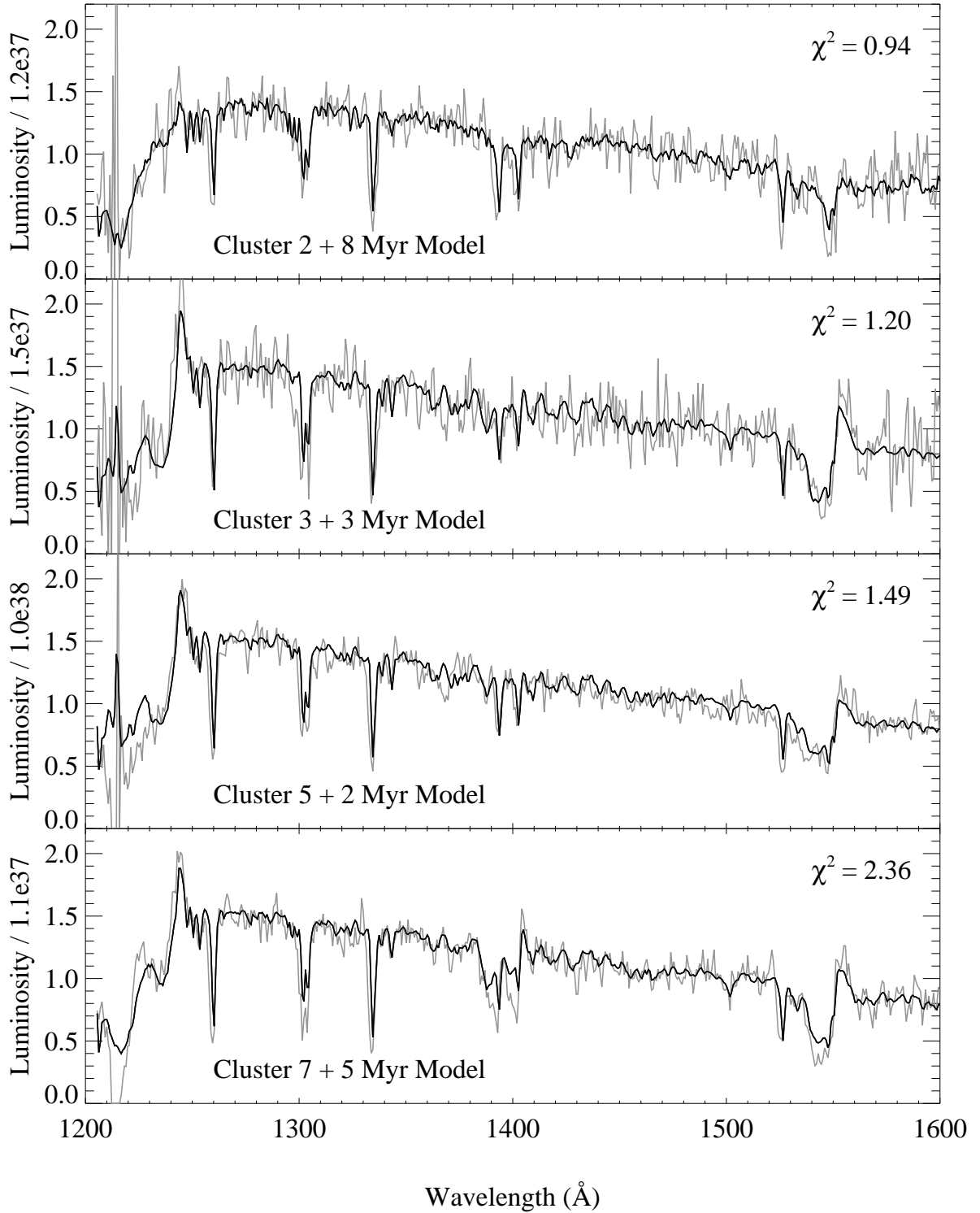


FIG. 7.— Dereddened spectra of the four brightest clusters 2, 3, 5, and 7 are shown in grey with their best fitting instantaneous burst models overplotted in black. Luminosity units are  $\text{ergs s}^{-1} \text{Å}^{-1}$ . The reduced  $\chi^2$  values of the fit are labeled on the plots for reference.

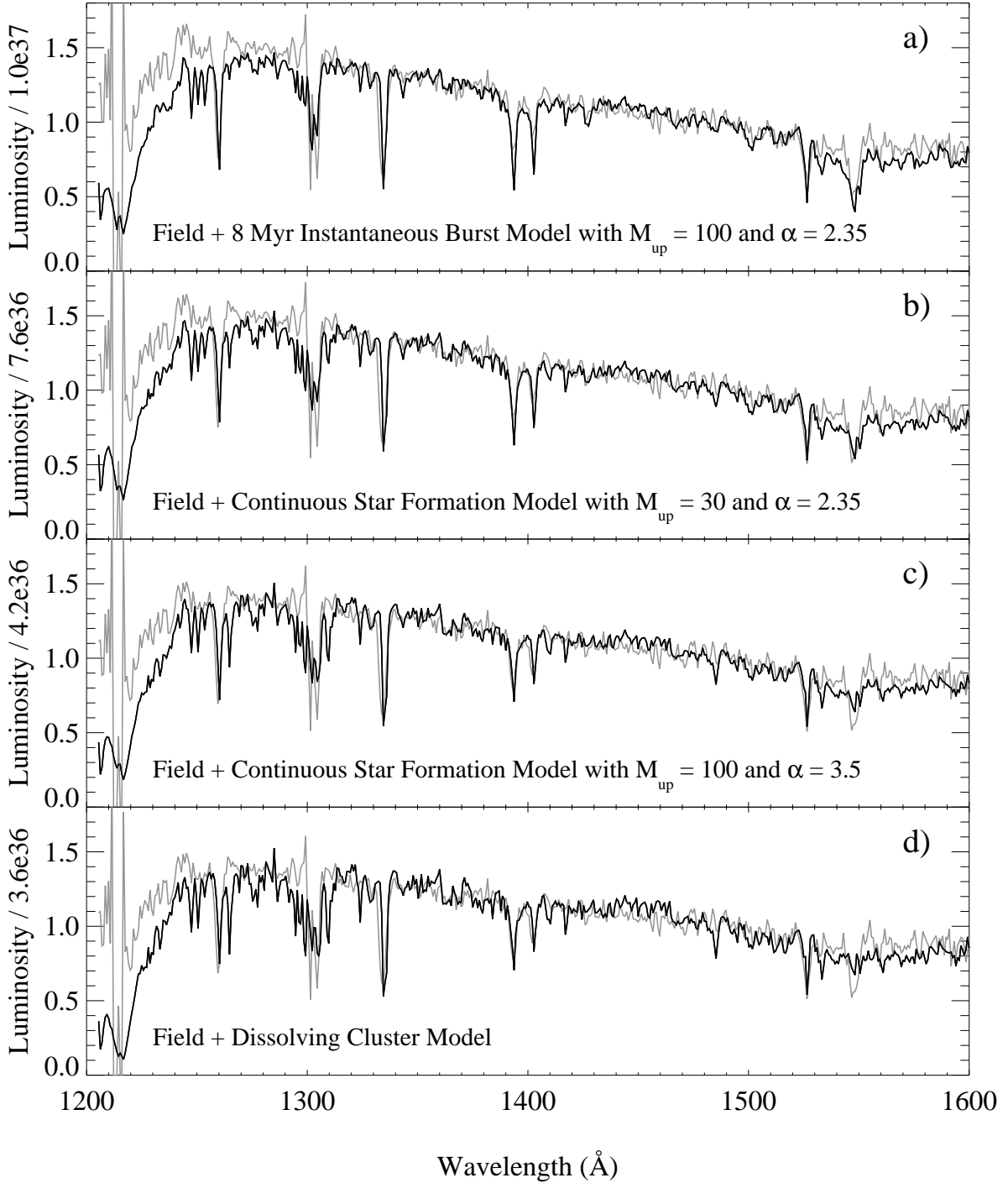


FIG. 8.— The total field spectrum is shown in grey with different models overplotted in black: a) an 8 Myr old instantaneous burst model with a Salpeter IMF extending up to  $100 M_{\odot}$  b) a continuous star formation model with a Salpeter IMF slope ( $\alpha = 2.35$ ) and an upper mass cut-off of  $M_{up} = 30 M_{\odot}$  c) a continuous star formation model with  $\alpha = 3.5$  and  $M_{up} = 100 M_{\odot}$  d) 100 Myrs of continuous star formation with 10 Myrs of continuous star formation subtracted off. This model represents a “dissolving clusters” scenario (see § 6.2.) Luminosity units are  $\text{ergs s}^{-1} \text{Å}^{-1}$ .

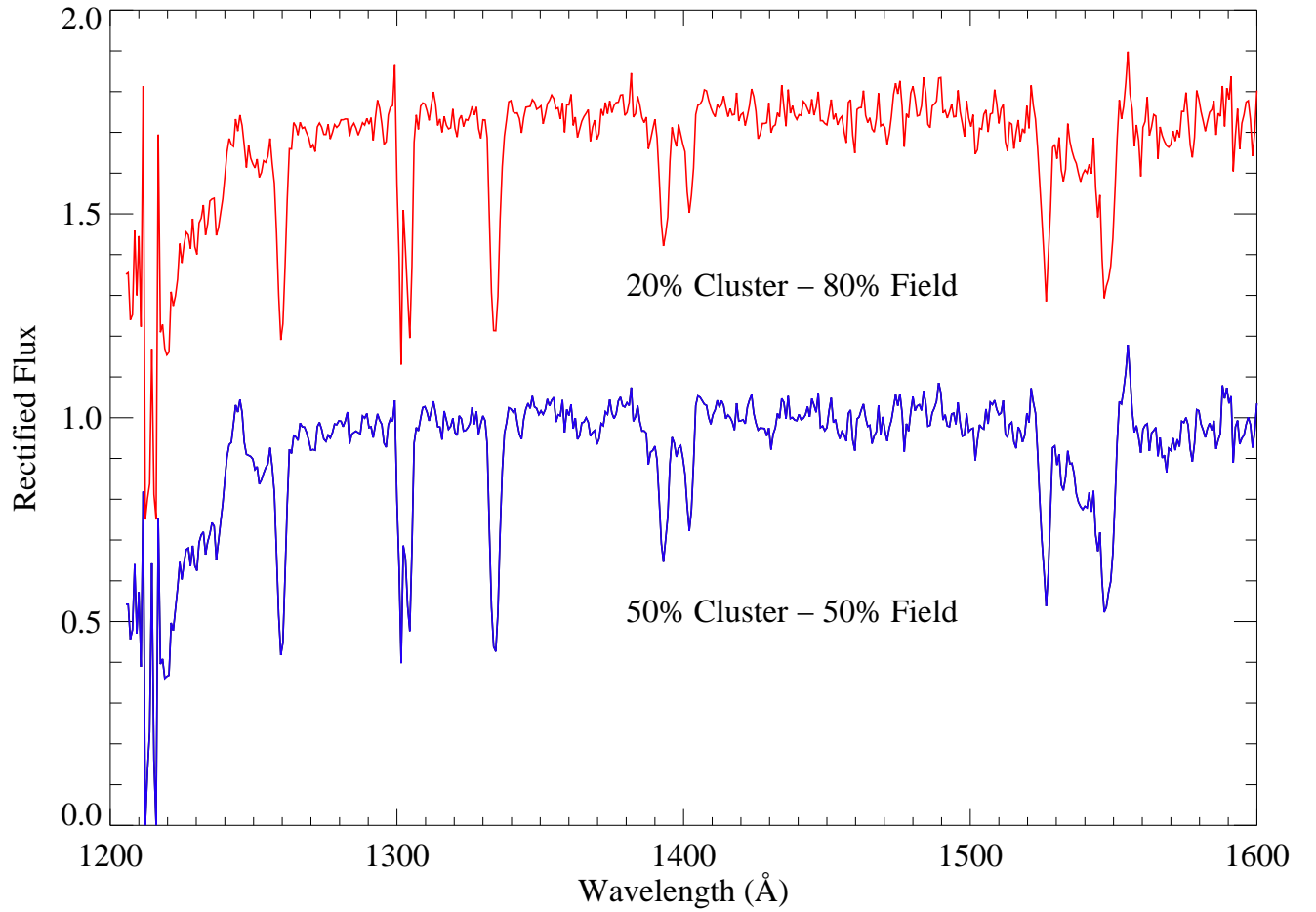


FIG. 9.— We have constructed two spectra to simulate a spatially integrated spectrum of NGC 5253. These bracket the observed values for the fraction of UV light coming from resolved sources: 20% clusters – 80% field (top) and 50% clusters – 50% field (bottom). These template spectra provide a much more accurate benchmark for comparisons with the spatially integrated spectra of high redshift galaxies than previously available high resolution starburst spectra, which are primarily of individual clusters.

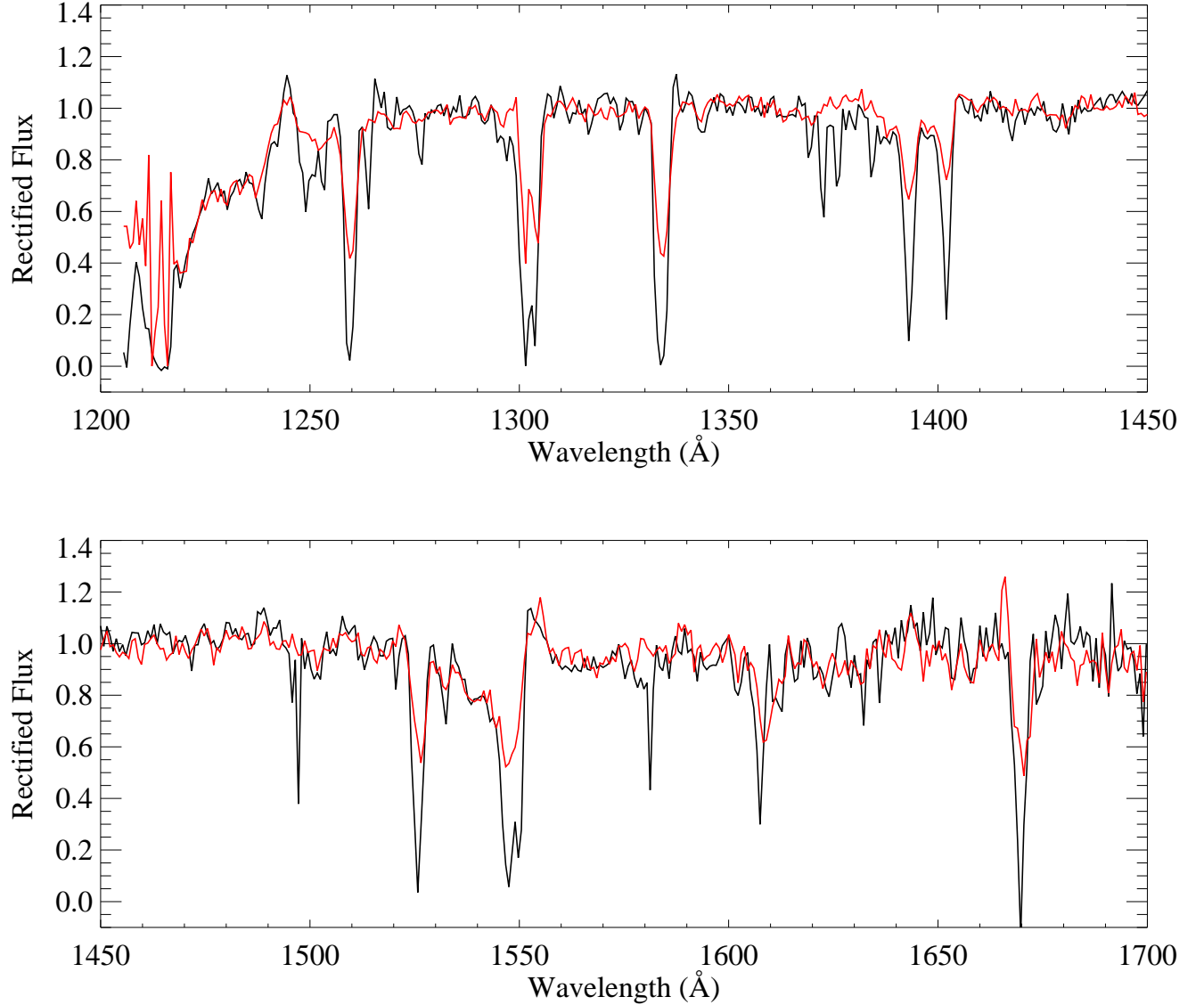


FIG. 10.— The spectrum of MS 1512-cB58, a gravitationally lensed  $z = 2.73$  starburst, is shown in black (Pettini et al. 2000) with the 50% cluster–50% field template spectrum of NGC 5253 overplotted in red. Note the excellent agreement of the continuum and line profiles of the stellar wind features, N V  $\lambda 1240$ , Si IV  $\lambda 1400$ , and C IV  $\lambda 1550$ , with the exception of the line cores, which are interstellar in origin. All of the interstellar features of cB58 are much deeper than those of the template spectrum (and much broader, given that the interstellar lines of NGC 5253 are blended with intervening Milky Way lines); this is probably a result of the greater covering factor of the gas in the cB58 spectrum, and of the hydrodynamical consequences of the galaxy’s high star formation rate. The lines present only in the cB58 spectrum near 1375, 1500, and 1580 Å are intervening absorption features.

TABLE 1  
OBSERVED PROPERTIES OF THE STELLAR CLUSTERS.

Cluster <sup>a</sup>	Pixels <sup>b</sup>	S/N <sup>c</sup>	$R_{eSTIS}(\text{pc})^{\text{d}}$	$R_{eF170W}(\text{pc})^{\text{e}}$	$F_{STIS}^{\text{f}}$	$F_{F170W}^{\text{g}}$	$\beta^{\text{h}}$
2	21	8	0.68	1.69	$7.95 \times 10^{-17}$	$1.04 \times 10^{-15}$	-1.11
3	23	7	0.58	0.96	$6.69 \times 10^{-17}$	$1.64 \times 10^{-15}$	-1.27
5	27	14	2.38	4.43	$2.53 \times 10^{-16}$	$1.08 \times 10^{-15}$	0.50
7	29	15	0.57	0.73	$3.42 \times 10^{-16}$	$1.01 \times 10^{-15}$	-1.11
8	13	8	0.17	...	$7.03 \times 10^{-17}$	...	0.13
9	23	9	0.59	...	$9.74 \times 10^{-17}$	...	-0.62
10	25	7	0.55	...	$6.64 \times 10^{-17}$	...	-1.14
11	27	6	0.70	...	$3.86 \times 10^{-17}$	...	-1.87

<sup>a</sup>Cluster identification: for clarity we use the naming convention of Calzetti et al. 1997 for clusters 2, 3, and 5. We number the remaining clusters in order of decreasing brightness. The location of the clusters in the galaxy and relative to the slit is shown in Figures 1 and 2.

<sup>b</sup>Number of pixels summed up in the spatial direction for each cluster. See §3 for details.

<sup>c</sup>Median signal-to-noise of the extracted 1-dimensional STIS spectrum

<sup>d</sup>Half light radii in parsecs measured by fitting a gaussian to the cluster spatial profile in the STIS spectrum. These radii will underestimate the true value if the slit is not perfectly centered on the cluster. The value reported for Cluster 8 is for the bright point source (see §5.1).  $1 \text{ pc} \approx 0''.0625 \approx 2.56 \text{ pixels}$ .

<sup>e</sup>Half light radii in parsecs measured by fitting a two dimensional gaussian profile to clusters in the WFPC2 F170W image. Clusters 8, 9, 10, & 11 are too faint to be detected in the image.

<sup>f</sup>Flux in  $\text{ergs s}^{-1} \text{ cm}^{-2} \text{ \AA}^{-1}$  at  $1500 \text{ \AA}$  measured from the STIS spectrum. These values have not been corrected for reddening and slit losses.

<sup>g</sup>Flux in  $\text{ergs s}^{-1} \text{ cm}^{-2} \text{ \AA}^{-1}$  measured from photometry of our WFPC2 F170W image. Clusters 8, 9, 10, & 11 are too faint to be detected in the image.

<sup>h</sup>Observed power law index of the UV continuum ( $F \propto \lambda^\beta$ ) over the wavelength range  $1240 - 1600 \text{ \AA}$ . See §3 for details.

TABLE 2  
DERIVED PROPERTIES OF THE STELLAR CLUSTERS.

Cluster	$\beta_i^a$	$E(B-V)^b$	$L_{STIS}^c$	$L_{F170W}^d$	Age(Myr) <sup>e</sup>	Mass( $M_\odot$ ) <sup>f</sup>	Reduced $\chi^2$ <sup>g</sup>
2	-1.55	0.16	$7.41 \times 10^{35}$	$1.17 \times 10^{37}$	$8^{+2.6}_{-0.9}$	$1 \times 10^4$	0.94
3	-1.71	0.14	$4.87 \times 10^{35}$	$1.48 \times 10^{37}$	$3^{+0.9}_{-0.9}$	$4 \times 10^3$	1.20
5	0.06	0.42	$2.56 \times 10^{37}$	$1.00 \times 10^{38}$	$2^{+0.7}_{-0.8}$	$4 \times 10^4$	1.49
7	-1.55	0.16	$3.14 \times 10^{36}$	$1.11 \times 10^{37}$	$4^{+1.1}_{-0.7}$	$5 \times 10^3$	2.36
8	-0.29	0.36	$4.23 \times 10^{36}$	...	$8^{+5.9}_{-1.2}$	$> 5 \times 10^3$	1.46
9	-1.07	0.26	$1.86 \times 10^{36}$	...	$1^{+2.2}$	$> 9 \times 10^2$	1.27
10	-1.48	0.18	$6.82 \times 10^{35}$	...	$8^{+6.5}_{-1.2}$	$> 7 \times 10^2$	1.33
11	-2.31	0.05	$1.17 \times 10^{35}$	...	$6^{+1.2}_{-1.5}$	$> 1 \times 10^2$	1.57

<sup>a</sup>Power law index of the UV continuum ( $F \propto \lambda^\beta$ ) over the wavelength range 1240 – 1600 Å after correcting for a foreground Milky Way reddening of  $E(B-V) = 0.05$ .

<sup>b</sup>Reddening derived using the starburst obscuration curve, assuming an intrinsic slope of  $\beta = -2.6$ .

<sup>c</sup>Extinction corrected luminosity at 1500 Å in ergs  $s^{-1} \text{Å}^{-1}$  measured from the STIS spectrum, with no attempt made at aperture corrections. We use the starburst obscuration curve and the  $E(B-V)$  values quoted here.

<sup>d</sup>Extinction corrected luminosity at 1500 Å in ergs  $s^{-1} \text{Å}^{-1}$  derived from photometry of a WFPC2 image in the F170W filter. The observed slope of the UV continuum is used to correct the flux given in Table 1 from the effective wavelength of the F170W bandpass to 1500 Å. Clusters 8, 9, 10, & 11 are too faint to be measured in the image.

<sup>e</sup>Age derived from the best fitting *STARBURST99* instantaneous burst model with error bars representing the 90% confidence interval. See § 4.3 for details.

<sup>f</sup>Mass derived by comparing the observed luminosity to that predicted by *STARBURST99* for a  $10^6 M_\odot$  cluster of the appropriate age. For clusters where photometry was unavailable, the mass is shown as a lower limit, because the aperture corrections are unknown. Because of uncertainties in the dust geometry and the lower mass cutoff of the IMF, all of our derived masses may be underestimates by factors of a few. See § 5.1 for details.

<sup>g</sup>The reduced  $\chi^2$  value of the fit of the model to the cluster spectrum. See § 4.3 for details.



TABLE 3  
OBSERVED PROPERTIES OF THE FIELD REGIONS.

Region <sup>a</sup>	Pixels <sup>b</sup>	S/N <sup>c</sup>	Size(pc <sup>2</sup> ) <sup>d</sup>	$F_{STIS}$ <sup>e</sup>	$\beta^f$
Field 1	127	12	80.8	$2.17 \times 10^{-16}$	-1.08
Field 2	161	16	102.4	$3.47 \times 10^{-16}$	-1.20
Field 3	167	18	106.2	$4.21 \times 10^{-16}$	-1.09
Field	455	27	289.4	$9.80 \times 10^{-16}$	-1.12

<sup>a</sup>Designations given to the three different field regions. The row labeled “Field” refers to the combined values of the three regions. The location of these regions along the slit is shown in Figure 2.

<sup>b</sup>Number of pixels summed up in the spatial direction for each field region. See §3 for details.

<sup>c</sup>Median signal-to-noise of the extracted 1-dimensional STIS spectrum.

<sup>d</sup>Area in parsecs<sup>2</sup> of each field region.  $1'' \approx 16$  pc.

<sup>e</sup>Flux in  $\text{ergs s}^{-1} \text{cm}^{-2} \text{\AA}^{-1}$  at 1500  $\text{\AA}$  measured from the STIS spectrum. These values have not been corrected for reddening.

<sup>f</sup>Observed power law index of the UV continuum ( $F \propto \lambda^\beta$ ) over the wavelength range 1240 – 1600  $\text{\AA}$ . See §3 for details.

TABLE 4  
BEST FITTING FIELD MODELS

Star Formation Law	$M_{up}$ <sup>a</sup>	$M_{low}$ <sup>b</sup>	$\alpha$ <sup>c</sup>	Age(Myrs) <sup>d</sup>	$\beta_m$ <sup>e</sup>	$E(B-V)$ <sup>f</sup>	SFR	Reduced $\chi^2$ <sup>h</sup>
Instantaneous	100	1	2.35	8	-2.7	0.18	...	1.8
Continuous	30	1	2.35	50	-2.5	0.15	1.3	2.0
Continuous	100	1	3.50	50	-2.1	0.08	3.0	2.2

<sup>a</sup>Upper mass cut-off of the IMF.

<sup>b</sup>Lower mass cut-off of the IMF.

<sup>c</sup>Power law slope of the IMF ( $\Phi \propto \int m^{-\alpha} dm$ ).

<sup>d</sup>Age in Myr of the model used.

<sup>e</sup>Power law index of the UV continuum ( $F \propto \lambda^\beta$ ) of the model over the wavelength range 1240 – 1600 Å.

<sup>f</sup>Reddening derived using the starburst obscuration curve from the difference in the model slope,  $\beta_m$ , and the observed slope of the field after correction for a small amount of foreground reddening ( $\beta = 1.56$ ). See §8 for details.

<sup>g</sup>Implied star formation rate in  $M_\odot \text{ yr}^{-1} \text{ kpc}^{-2}$ .

<sup>h</sup>The reduced  $\chi^2$  value of the fit of the model to the field spectrum. See § 4.3 for details.